Nuclear Materials and Energy 39 (2024) 101647

Contents lists available at ScienceDirect

Nuclear Materials and Energy

journal homepage: www.elsevier.com/locate/nme

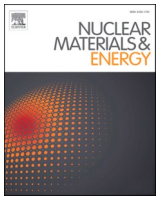

Multiscale computational study to predict the irradiation-induced change in engineering properties of fusion reactor materials

Salahudeen Mohamed [a,b,d,*], Giacomo Po [c], Rhydian Lewis [a], Perumal Nithiarasu [a]

[a] Zienkiewicz Institute for Modelling, Data and AI, Swansea University, Swansea SA1 8EN, UK
[b] Culham Centre for Fusion Energy, Culham Science Centre, Abingdon, Oxon, UK
[c] Department of Mechanical and Aerospace Engineering, University of Miami, Coral Gables, FL 33146, USA
[d] Institute for Applied Materials, Karlsruhe Institute of Technology (KIT), Eggenstein-Leopoldshafen, 76131 Karlsruhe, Germany

ARTICLE INFO

Keywords:
Neutron irradiation
Neutronics
Finite element
Yield stress
Dislocation dynamics
Thermo-mechanical behaviour

ABSTRACT

In this study, we address the impact of irradiation conditions in a tokamak on the engineering properties of materials, leading to potential degradation of in-vessel components over their lifecycle. Our approach involves a predictive model for irradiation-induced damage, employing a multiscale computational framework. This framework integrates various simulation techniques, including Monte Carlo-based neutronics (OpenMC), dislocation dynamics (DD) using MoDELib, and finite element analysis (FEA) with Code_Aster. This integration offers a versatile solver capable of analysing tokamak components exposed to different irradiation doses and temperature conditions.

To showcase the utility of this multiscale computational framework, we present a case study focused on tungsten monoblock designs. We assess the failure probabilities of these designs at different stages of their lifecycle. Neutron heating and damage energy values are obtained from OpenMC neutronics simulations. The neutron heating values serve as volumetric heat sources for the FEA thermal simulation. We calculate the displacement per atom (dpa) across the monoblock at various full power days (day 0, day 100, and day 1000) using the damage energy values. The irradiation-induced defect densities, dependent on temperature and dpa, are inputs to DD microstructural simulations performed on the representative volume element (RVE) using MoDELib. This allows us to obtain the yield stress of the material. Subsequently, the thermal fields from the FEA thermal simulation, along with the dpa and temperature-dependent yield stress from the DD simulation, are implemented for FEA mechanical simulations.

To evaluate the failure probability of the monoblock designs at different stages of their lifecycle, we conduct an SDC-IC assessment, incorporating a plastic flow localization rule within the current framework. This comprehensive approach provides insights into the thermo-mechanical behaviour of in-vessel components subjected to neutron irradiation, offering a predictive capability for assessing their performance over time.

Introduction

A critical challenge in the development and design of in-vessel components for tokamak, a type of fusion device, is the ability to withstand prolonged exposure to the fusion-induced high-energy neutron irradiation (14 MeV) and large thermal loads (up to 20 MW/m^2) while maintaining their structural integrity and thermal efficiency [1–3]. Due to the adverse irradiation conditions, in-vessel materials undergo degradation over their lifecycles [4–7]. Moreover, degradation occurs non-linearly based on the location in question relative to that of the neutron source due to non-uniform irradiation energies and dose rates, along with variations in temperature. This results in spatial and temporal variations in the evolution of the engineering properties of the material and in turn influence the overall operational performance of the tokamak [8,9]. For example, neutron irradiation reduces the fracture toughness of fusion-relevant materials. Such toughness reduction should be minimised in a structural component to avoid instability of the tokamak operation [10]. Moreover, the degradation in thermal conductivity of irradiated materials leads to steeper temperature gradients across the in-vessel components causing elevated surface temperatures and thermal stresses [11]. Thus, significantly irradiated components are prone to melting and cracking, which consequently reduces the lifespan of the tokamak.

* Corresponding author at: Institute for Applied Materials, Karlsruhe Institute of Technology (KIT), Eggenstein-Leopoldshafen, 76131 Karlsruhe, Germany.
E-mail address: Salahudeen.kunju@kit.edu (S. Mohamed).

https://doi.org/10.1016/j.nme.2024.101647
Received 1 February 2024; Received in revised form 29 March 2024; Accepted 30 March 2024
Available online 1 April 2024

Nomenclature

PKA	Primary knock on atom
SFT	Stacking fault tetrahedron
DFT	Density functional theory
FEA	Finite element analysis
DD	Dislocation Dynamics
RVE	Representative volume element
BCC	Body centered cubic
FCC	Face centered cubic
dpa	Displacement per atom
a	Lattice parameter
P_L	Mechanical stress
Q_L	Secondary stress
S_e	Yield stress
R_f	Reserve factor
NOC	Normal operating condition

The irradiation process involves the impingement of high-energy fast neutrons on plasma-facing components [12,13]. The subsequent interaction between atoms on the crystal lattice and neutrons creates Primary Knock-on Atoms (PKAs), which undergo collision cascades and lead to the formation of various nano and micro-scale level defects [14]. The major irradiation-induced defects are interstitials, vacancies, transmutation products, dislocation loops, precipitates, stacking fault tetrahedra (SFT), and voids [15–18]. These defects serve as an obstacle for the slip dislocations, resulting in an increase in yield stress, embrittlement and undesirable hardness, which changes the mechanical properties of the materials [19–22]. At the atomistic level, defects occur for a wide range of lengths and timescales, resulting in alteration of the mechanical properties of the material at the macro-scale, making irradiation damage a multiscale phenomenon.

The micro/nano scale defects produced in a component due to neutron irradiation contributes to the resistance to line dislocation motion at crystallographic planes, consequently results in the increase of hardness and yield stress. This influences the overall structural behaviour and intended operation of the component. In the earlier works, several experimental and numerical studies were carried out to investigate the hardness of irradiation induced defects on nuclear reactor materials and components [23–28]. In the case of experimental studies, the test specimens are irradiated in surrogated reactors, such as High Flux Isotope Reactor (HFIR) and Jōyō, with the microstructural defects analysed by means of Transmission Electron Microscopy (TEM) images [27]. In these studies, the hardness of the specimens as a function of irradiation-induced defects are measured. These experimental studies were crucial in shedding the light on the information regarding the defect types, defect sizes, and defect density of the nuclear reactor materials. Computational studies were on multiscale modelling with the primary aim to bridge different length scales to transfer the information regarding irradiation-induced defects [29,30]. Molecular dynamics simulations or ab-initio density calculations such as density functional theory (DFT) methods have been employed by many authors to obtain the thermodynamic behaviour of defects to provide information on higher scale models to quantify the mechanical parameters [31,32]. In a numerical study conducted by Dudarev et al. [33], the stress and strain field on the macro-scale of components is evaluated based on the microstructural defects induced by the high neutron irradiation of the component. For this, the microstructural evolution of the defects is estimated by means of density functional calculations and large-scale molecular dynamics simulations. The obtained defects are treated as source function in an integral equation and the stress, strain, and swelling are evaluated on the macro-scale of the component. A thermo-mechanical multiscale numerical study is carried out by Oude Vrielink et al. [34] to analyse the fracture probability assessment of the fusion relevant component based on the stress fields calculated. The mechanical behaviour of the component is modelled in terms of a crystal plasticity based microstructural model and the hardening parameters, due to irradiation, were calculated with cluster dynamics model. A multiscale framework is developed by Wang et al. [35] to investigate the influence of irradiation-induced defect evolution on the stress and yield stress of tungsten (W) components at the macroscale level. This is achieved by calculating the defect evolution parameters from the defect kinetic equations and these are implemented in the crystal plasticity finite element analysis (FEA) to study the macro-scale behaviour.

Most of the previous studies have successfully linked different scales of various modelling techniques and predicted the mechanical behaviour of test specimens based on the irradiation-induced defect information data. However, these studies didn't address the structural/thermal behaviour of the component over its lifecycle during operation due to the spatial and temporal variation in the engineering properties of the material. The present work addresses the following aspects:

- Component scale simulations, which account for the spatial variation in irradiation due to source location and shielding.
- Prediction of the material property evolution over their lifecycle and investigate the non-linear change in the performance of components.
- Acceleration of the iterative design cycle by accounting the changes in the space and time through automated parameterised workflow to model the influence of irradiation on materials.

Currently, the experimental campaigns on in-vessel materials are conducted by means of surrogate fusion radiation facilities, which cannot fully reproduce the real fusion environment of the tokamak. Moreover, sorting and down selecting the candidate designs of in-vessel components by means of experimental testing alone is expensive due to facility and time requirements. This process can be accelerated considerably through the development of a reliable predictive capability methodology, which evaluates the material behaviour by digitally emulating the fusion irradiation conditions. This also reduces the costs associated with performing physical experiments. The methods presented here has the flexibility to incorporate different types of defect data as a function of irradiation dose and temperature and extrapolate this information to a large-scale level component for predicting the thermal and mechanical behaviour and their evolution over a component's lifecycle. This enables the creation of a database of material properties, which vary with temperature and irradiation dose. Engineering simulations can use this non-linear data to assess an in-vessel component at various stages of its operation based on the neutron irradiation-induced defect data. The computational framework developed in the current work will be beneficial for the fusion community in the research and development of tokamak components as well as to investigate novel materials.

The methodologies implemented in the current work use Monte Carlo based neutronics, dislocation dynamics (DD), and FEA. During the PKA event, the neutron flux converts some of its kinetic energy into thermal energy resulting in the temperature rise on the component. To mimic this process, neutronic simulations are important to quantify the neutron heating values and it can be implemented to obtain the thermal loads for the DD and FEA simulations. Due to the lack of experimental neutron irradiated defect information under fusion energy conditions, models like DD are useful to extract the relevant parameters by simulating the actual interaction between the line dislocations and complex defect structures (e.g., precipitates, dislocation loops and interstitials) and transferring these parameters into an engineering scale component analysis. The crucial engineering properties like yield stress at various levels of the irradiation under fusion relevant conditions for different materials can be derived from the DD simulation to use within FEA simulations.

The paper is organised as follows: Section 2 describes the multiscale

computational framework, Section 3 reports the results obtained by utilising the developed methodology on a case study.

Multiscale computational framework

In the present work, a multiscale hierarchical computational predictive capability is developed to link the neutron irradiation-induced micro/nano scale defects response to the mechanical behaviour of tokamak components. Fig. 1 describes the implementation and coupling of the methodologies implemented. The letters (A)-(G) in the Fig. 1 denote various stages/components of the methodologies implemented in the current work. The neutron heating values from the Monte-Carlo based simulations from OpenMC v0.13.0 [36] (B, Fig. 1) are employed as thermal loads for the FEA in Code_Aster v14.4 (C) [37]. The damage energy obtained from the OpenMC simulation is used to calculate the displacement per atom (dpa), which in turn facilitates the implementation of dose dependent irradiation-induced defects as input for DD simulation (D, E). In fact, OpenMC is employed within Paramak v0.8.1 [38] and Code_Aster is within the Salome-Meca v2019.0.3 software package [37]. For the mechanical FEA simulation (F), elasto-plastic model, Von Mises plasticity model with isotropic hardening, is implemented. The yield stress and stress–strain data for the plasticity model is obtained from the DD simulation performed in the software 'Mechanics of Defect Evolution library' (MoDELib) (D, E, Fig. 1) on an uniaxially loaded 'Representative Volume Element' (RVE) for a given fusion relevant material with neutron irradiation-induced defects [39]. These packages are in turn linked together within VirtualLab 0.2.0 (Swansea University, UK), an open-source based platform developed by the co-authors of this paper. The multi-scale computational framework is released as an open-source project under the Apache 2.0 license and issued via Gitlab repository. The postprocessing is carried out in ParaView v5.11 [40]. In order to reproduce the numerical results reported in the current paper, the relevant numerical codes and tutorials are provided in the following Gitlab repository:

- https://gitlab.com/ibsim/virtuallab.
- https://virtuallab.readthedocs.io/en/docs/examples/Irradiation_damage.html.

Since the proposed multiscale computational framework consists of multiple interlinked parameters, uncertainty quantification can provide an estimation of its reliability. However, uncertainty quantification study is outside the scope of the current work. The framework developed in this work can also be employed to study fusion relevant phenomenon like tritium retention. The irradiation-induced defects can modify the tritium transport parameters and even create tritium traps, which consequently increases the tritium retention, and it is a safety concern [41]. Due to the modular nature of the multiscale computational framework, models like FESTIM (Finite Elements Simulation of Tritium in Materials) can be integrated, which has the capability to model the diffusion and trap of tritium in materials [42]. The resultant heat transfer calculated by FESTIM due to tritium retention can be employed for FEA mechanical simulation in Code_Aster in the current framework.

To understand the multiscale computational framework in the current work, a study has been carried out for a W monoblock from the divertor region of a tokamak. The geometrical dimensions of the monoblock is taken from the work of Lukenskas et al. [43]. The monoblock consists of W armour as the outer component, copper (Cu) as an interlayer and an inner CuCrZr cooling channel as shown in the Fig. 2a [44].

Neutronics simulation

During the nuclear fusion reaction, the neutrons are produced by the fusion of deuterium and tritium nuclei. These neutrons will travel from the site of the reaction in the plasma and interact with in-vessel plasma facing components. In these consequential reactions, charged particles, gamma rays and secondary neutrons are produced, which results in the PKAs of nuclides. The knocked nuclides and the charged particles travel through the material for a short range and the resultant kinetic energies are converted into thermal energy. However, the neutrons and the gamma rays move in the materials for a longer range and exchange their kinetic energy to thermal energy through elastic and inelastic collisions with the material atoms. The thermal energies obtained from these kinetic energies are called nuclear heat. In this study, the authors have obtained the nuclear heating values and damage energy deposited for PKAs by means of Monte-Carlo method. The damage energy is the

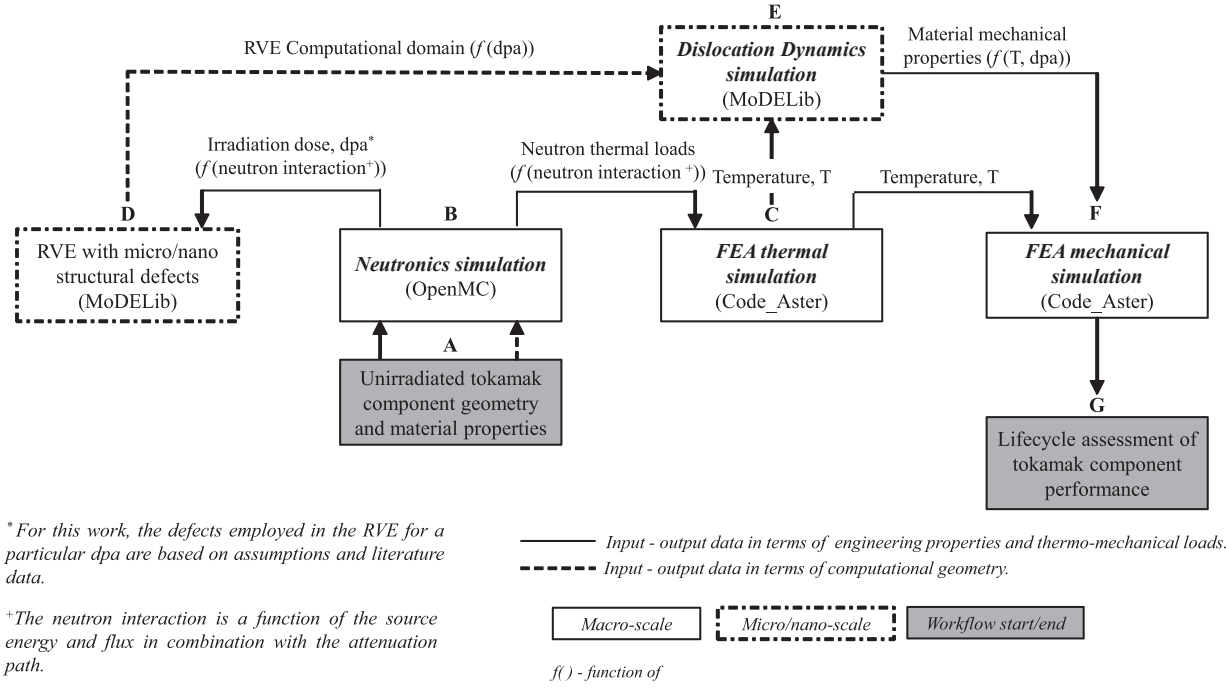

Fig. 1. Schematic diagram of the workflow for the developed platform.

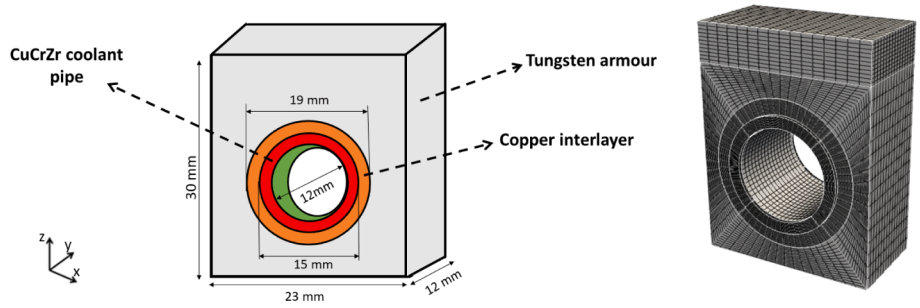

(a) (b)

Fig. 2. (a) Schematic representation of W monoblock (b) Computational mesh of the W monoblock.

available kinetic energy to create atomic displacements. This energy for an incident particle is calculated as the total incident particle energy minus the energy lost to interaction with the atoms [45]. For this, OpenMC (B, Fig. 1) is employed, which implements Monte-Carlo code to model the neutron transport, heating, and PKAs in fusion conditions. The nuclear heating values generated from the reactions are computed using nuclear data processing code, NJOY, implemented within OpenMC package. To calculate the dpa across the tokamak components, the damage energy per source particle is obtained based on the Material Table (MT) = 444 within the HEATR module of NJOY in OpenMC. More details on the methodology used in OpenMC can be found in Romano et al. [36].

The OpenMC based Monte Carlo simulation is carried out on the W monoblock under fusion energy conditions. The ENDFB-7.1 nuclear data from the NNDC OpenMC distribution is employed for the neutronics calculation (B, Fig. 1) [36]. The monoblock CAD geometry is created using CadQuery v2.0 [38] and is converted to OpenMC neutronics model by means of DAGMC v3.2.1 [46]. To perform the simulation in OpenMC, the cross-section and mass density of the materials in the monoblock are required. The cross-sections of the materials are obtained from the ENDFB-7.1 nuclear data while the mass densities are implemented from the ITER database [47]. The simulation is performed for 500,000 particles per batch and a total of 50 batches are simulated from an isotropic fusion energy source with 14 MeV monoenergetic neutrons. The scored neutron heating and damage energy values are tallied onto the OpenMC mesh of the monoblock. Since the tallied results of neutron heating are in electron Volts (eV), it is multiplied by the source strength of 1 GW fusion DT plasma and divided by the volume of the corresponding cells to obtain the neutron heating values in terms of $W{\cdot}m^{-3}$. From the tallied damage energy results, the dpa across the monoblock is calculated based on Norgett-Robinson-Torrens displacement per atom (NRT-dpa) model [48]. The dpa calculated in the study is an approximation, which is calculated in terms of atom-based estimate of material exposure to neutron irradiation in fusion-relevant conditions.

Dislocation dynamics simulation

At macro-scale levels, it has been shown experimentally for neutron-irradiated materials that there is an increase in yield stress in metals such as aluminium (Al), Cu, nickel (Ni), W, and zirconium (Zr). This is due to the interaction of dislocations at the slip planes with the defects, which cause irradiation-induced hardening. The dislocations are the plastic deformation carriers inside a crystal lattice, and they interact with defects and other line dislocations resulting in annihilation and rearrangement of line dislocations, which consequently changes the overall microstructural configuration state with respect to the initial microstructure. To understand these complex dislocation–defect interaction mechanism at micro/nano scales and mimic the irradiation-induced hardening phenomena, DD models are used. The changes to important engineering parameters, such as yield stress, are obtained from DD simulations to be used for designing and conducting experimental tests on a large-scale component. Therefore, in this study, the authors have employed the DD code, MoDELib, to analyse the dislocation motion and its evolution due to the interaction with the neutron irradiation-induced defects (D, E, Fig. 1). The DD code is based on phenomenological mobility law and more details on the code can be found in Po et al. [39]. The DD simulations are performed on an RVE of tokamak component materials containing neutron irradiated-induced defects (Fig. 3) with uniaxial loading in terms of strain rate at a certain temperature to obtain yield stress and stress–strain data. The DD model inputs regarding the neutron irradiation-induced defects are implemented in terms of density and geometric dimension. This information has been gathered from the ab initio calculations and experimental analysis conducted in the previous studies [12,49,50]. This process would need to be repeated for each of the materials contained within the component being studied.

In this study, RVEs of BCC W and FCC Cu with defects are employed for the DD simulations (D,E, Fig. 1). DD codes can currently only analyse single crystalline solids with capabilities to analyse alloys (like CuCrZr) being under development. The RVE for the DD simulation is embedded with neutron irradiated-induced defects, which reproduces the irradiated state of W and Cu. The material properties of W and Cu implemented in the DD simulation are shown in Table 1.

DD simulations are performed on the single crystal W and Cu RVEs to obtain the yield stress and stress–strain data to use with the FEA. Different W RVEs, which incorporate the neutron irradiation-induced defects as a function of dpa are considered for the DD simulation as shown in the Fig. 4. These RVEs represent the degradation of a fusion reactor in-vessel component at different stages of the lifecycle during its operation. For lower dpa, RVEs with only line dislocations are considered to represent the irradiated W armour. Due to the prolonged period of operation, the W armour is degraded due to the neutron irradiation, which undergoes higher dpa with the formation of defects such as dislocation loops and precipitates. Therefore, dislocation loops, precipitates, and line dislocations are employed for the RVEs (Fig. 4 b and c) as the initial microstructure to represent higher dpa. For the Cu RVE, two different dose dependent states are considered. For the lower dpa state, Cu RVE with only line dislocations are analysed using DD while for the higher dpa, line dislocations SFTs, and dislocation loops are included as defects. For this work, as previously noted, parameters such as the defects' size and densities have been taken from literature.

The line dislocations at the crystallographic slip planes interact with the defects and among themselves due to the elastic stress fields. The resultant stress fields are implemented in the mobility law to analyse the temporal evolution of the line dislocation configuration. In the present study, the dislocation loops are $\langle 1\,1\,1 \rangle$ glissile loops distributed at the

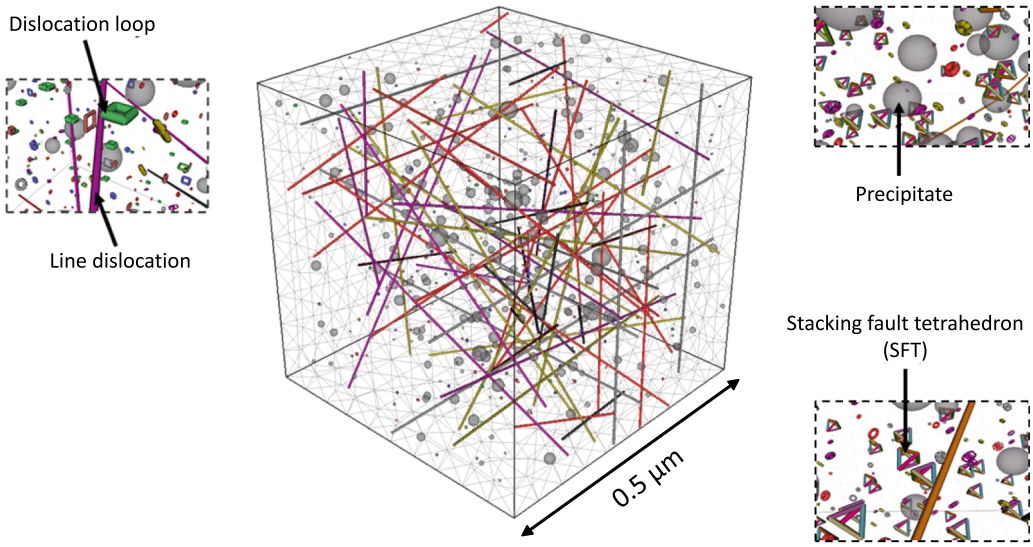

Fig. 3. RVE of fusion-relevant material with neutron irradiation-induced defects for DD simulation.

Table 1
Material properties of the W monoblock components used for the DD simulations [39].

Property	Symbol	Unit	Value	
			W	Cu
Melting temperature	T_m	[°C]	3,422	1,358
Lattice constant	A	[nm]	0.3160	0.3610
Burgers vector	B	[nm]	0.2722	0.2566
Shear modulus	*G*	[MPa]	161×10^9	48×10^9
Poisson ratio	N	[-]	0.28	0.34
Mass density	ρ	[kg/m^3]	19,250	8,940

slip planes. In the case of precipitates, it acts as the resistance to the dislocation motion and contributes to the additional stress in the material. The precipitates are modelled as spherical inclusions in DD simulation based on the Eshelby inclusion theory [51]. The stress fields of inclusions are responsible for the interaction between line dislocations and precipitates. The stress fields of inclusions are implemented in the DD code employing transformation strain (ε_T), which are calculated based on the difference in the lattice constants between matrix (a_m) and inclusion (a_{inc}) as shown in equation (1).

$$\varepsilon_T = \frac{a_{inc} - a_m}{a_{inc}} \quad (1)$$

The lattice constant of W (a_m) and rhenium (Re) precipitate (a_{inc}) are taken as 0.316 nm and 0.276 nm, respectively [52]. The inclusions with a mean diameter of 30 nm are distributed at the crystallographic slip planes of the W RVE along with the line dislocations and dislocation loops. For the current study, the precipitates, in terms of inclusions, are modelled as impenetrable and therefore they cannot be sheared.

The most common type of defects observed in W are dislocation loops, precipitates, and voids [12,50]. In the study carried out by Dürrschnabel et al. [12], TEM images of a W sample at 1.25 dpa are investigated following neutron irradiation. They observe defects like dislocation loops of size up to 10 nm and precipitates like Re and Osmium (Os) with sizes less than 10 nm. In the study conducted by Koyanagi et al. [50], the microstructural evolution of neutron irradiated single crystal W is analysed by means of TEM at 0.03–4.6 dpa. Based on their investigation, the dominant microstructural defects observed are dislocation loops with a size in the range of 1.3–4.6 nm. At higher dpa, precipitates of transmutation products such as Re and Os with size ranging between 30 nm and 37 nm are noticed. Hu et al. [27] have reported the irradiation-induced defect densities in W samples that were tested in the HFIR reactor. They have observed dislocation loop densities in the range of $.01 \times 10^{22}$ m^{-3} -5×10^{22} m^{-3} with sizes between 2.9 nm and 6.27 nm for dpa less than 1.62 dpa. In the same study [27], precipitates densities in the range of 3.6×10^{22} m^{-3} -8.6×10^{22} m^{-3} are reported at dpa greater than 1.62 dpa with sizes between 16 nm and 20

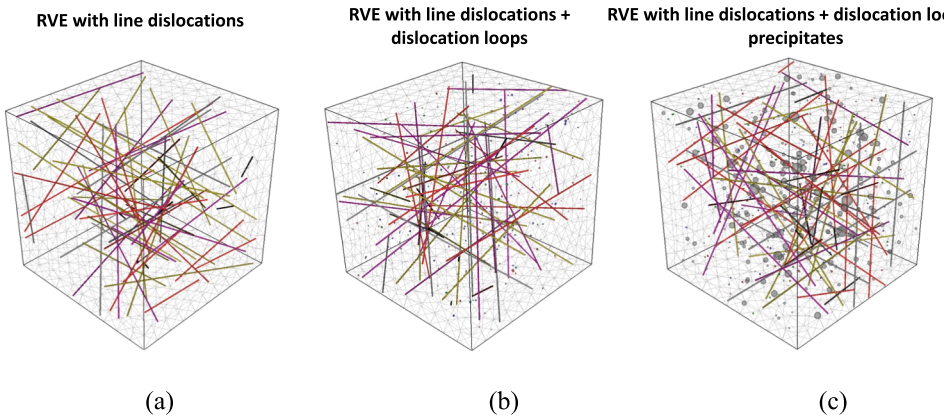

Fig. 4. Initial microstructure of different W RVEs with neutron irradiation-induced defects (a) RVE with line dislocations to represent lower dpa (b) & (c) RVE with line dislocations, dislocation loops and precipitates to represent higher dpa.

nm. In the experimental and numerical study performed by Bonny et al. [26], dislocation loop density between 1×10^{21} m^{-3} -2×10^{22} m^{-3} is reported at 0.1 dpa. Neutron irradiation on Cu mainly produces defects such as dislocation loops and SFTs. In the study by Eldrup et al. [53], during neutron irradiation on OHFC Cu, the defect cluster density increases proportional to the irradiation dose and saturates to a density of 1.3×10^{24} m^{-3} at 0.1 dpa. Most of the defect cluster density in irradiated Cu is SFT when compared to the dislocation loop and the size of the SFTs is the range of 2–3 nm [53]. SFT density of $2-4 \times 10^{23}$ m^{-3} and dislocation loop density of 5×10^{21} m^{-3} are reported by Edwards et al. [54] in a neutron irradiation experiment on Cu at 0.01 dpa. At temperatures between 20 °C and 180 °C, defect density in Cu is independent of the irradiation temperature [55,56]. While at irradiation temperature between 180 °C and 450 °C, the defect density decreases by around three orders of magnitude [57].

In the DD simulation, the present work has employed irradiation-induced defect density for certain irradiation temperature and dpa based on the previous experimental and modelling studies, which are reported by several authors [26,27,53–55,57]. In the case of W, dislocation loops and precipitates are modelled in the current study for DD simulation while the voids are not included in the current DD code since it is under development for further validation. Future studies are needed with the focus on the inclusion of void defect features on the basis of the current multi-scale computational framework. The defect densities (dislocation loop and precipitate) in the W RVE are selected based on the data from Hu et al. [27] and Bonny et al. [26] since these studies have reported defect density values for a range of temperatures and dpa as depicted in Fig. 5. Due to the few and low scatter of data of W on irradiation-induced defect density for a wide range of dpa and temperature, general trend of the defect density as a function of dpa and temperature is not known. Therefore, DD simulations are performed based on the neutron irradiation defect densities on W RVE for different irradiation temperature and dpa based on Fig. 5. The defect density values could be replaced in the future by improved experimental values or using a theoretical model.

In the case of Cu, SFT density in irradiated Cu is higher than the dislocation loop density and the defect cluster density, comprising SFT and dislocation loops, are distributed at the slip planes in the ratio of 9:1 (90 % SFT, 10 % dislocation loops) according to Eldrup et al. [53]. The defect cluster density for Cu, as shown in Fig. 6, is obtained from the studies by Zinkle [58] and Eldrup et al. [53]. It should be noted that the Cu defect density values at 70 °C are obtained from the study by Eldrup et al. [53] as a function of dpa (Fig. 6). The remaining defect density values as a function of dpa for other temperatures (250 °C-400 °C) are calculated and plotted based on the normalised defect density values reported in the study by Zinkle [58].

The defects are distributed in the W and Cu RVE, of size 0.5 μm, based on the log normal probability distribution function as shown in Fig. 3. For W material, the initial line dislocation density of 1×10^{14} m^{-2} is used and the initial microstructure of the W RVE, consists of precipitates, dislocation loops of family of ⟨1 1 1⟩ glissile loops and line dislocations, employed in the DD simulation. Dislocation loops of size 3.37 nm and precipitates of size 30 nm are implemented for W RVE. For the Cu RVE, an initial line dislocation density of 1×10^{14} m^{-2} is used. SFTs of size 2.5 nm and dislocation loops of size 3 nm are employed as neutron irradiation defects as shown in Fig. 6.

FEA thermal simulation

Fig. 2 a depicts the computational domain of the W monoblock employed in the current study for the FEA simulations. A total of 63,258 linear hexahedral elements are used for discretizing the monoblock as shown in Fig. 2 b and Table 2. Code_Aster is implemented to solve the heat equation to obtain the temperature field. For the FEA thermal simulation (C, Fig. 1), the neutron heating values from the neutronics simulation (B, Fig. 1) are assigned as the volumetric heat source for the monoblock. Plasma heat load of 10 MW·m^{-2} is imposed at the top surface of monoblock. The effect of the coolant is modelled based on similar approach to that carried out for modelling of the ITER cooling system [59]. The wall-temperature dependent heating curve is calculated using a combination of Sieder–Tate correlation for single phase and Thom–CEA correlation for nucleate boiling, which depend on properties of the coolant, mainly its temperature, velocity, and pressure [60,61]. This is then applied as a temperature dependent heat flux boundary condition in Code_Aster. Coolant temperature of 150 °C, velocity of 16 m/s and pressure of 5 MPa are implemented in the current work [60,61]. The thermal properties (specific heat, thermal conductivity, thermal expansion coefficient) for W armour, Cu interlayer and CuCrZr coolant pipe are obtained from the literature [47,53,62–69]. In particular, the thermal conductivity of W armour, Cu interlayer and CuCrZr coolant is plotted in Fig. 7 and Fig. 8 using previous study data [47,53,62–69]. The current study has not implemented any modelling technique to calculate thermal conductivity based on irradiation-induced defect features. However, mathematical techniques can be integrated into the current framework to evaluate thermal conductivity in terms of irradiation-induced defect density and size. The thermal field from FEA thermal simulation (C, Fig. 1) is implemented in the DD simulations (E, Fig. 1) on RVE of fusion relevant materials to obtain the dpa and temperature dependent yield stress and stress–strain data. The results from DD simulation (E, Fig. 1) and FEA thermal simulation (C, Fig. 1) are used for FEA mechanical simulation (F, Fig. 1) to analyse the thermally induced stress across the components.

FEA mechanical simulation

For the mechanical FEA simulation (F, Fig. 1), temperature values obtained from the FEA thermal simulation (C, Fig. 1) are employed along with the mechanical loads as boundary conditions. Translational displacement constraints are assigned at the bottom nodes of W armour. A wall pressure of 5 MPa is used at the cooling channel to reproduce the water flow by force convection. Elasto-plastic model, Von Mises plasticity with isotropic hardening, is employed for W armour, Cu interlayer

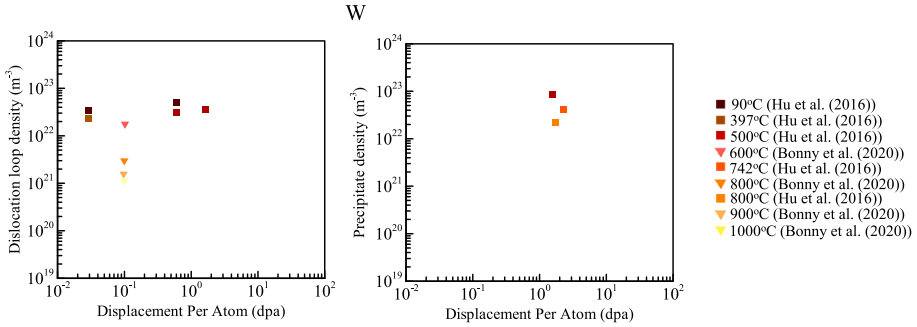

Fig. 5. Neutron irradiation-induced defect density employed in DD simulation for W RVE.

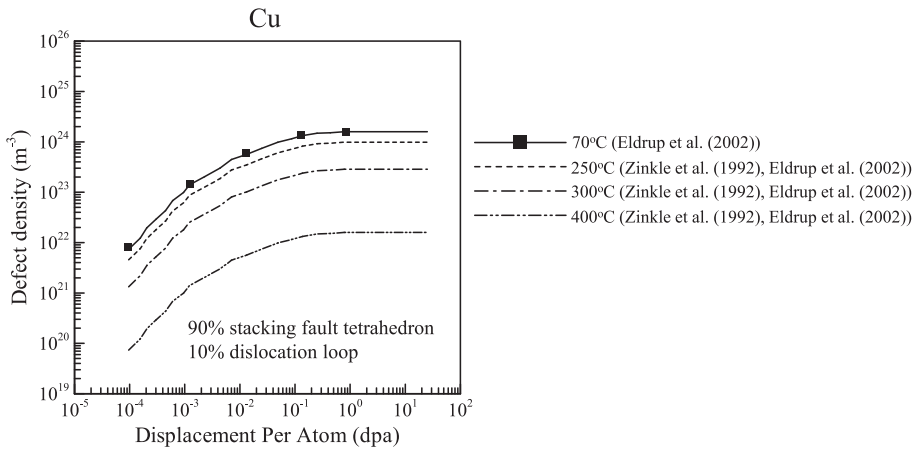

Fig. 6. Neutron irradiation-induced defect density employed in DD simulation for Cu RVE.

Table 2
Number of hexahedral elements employed in the W monoblock.

Component	Hexahedral elements
W	19,200
Cu	16,834
CuCrZr	27,074

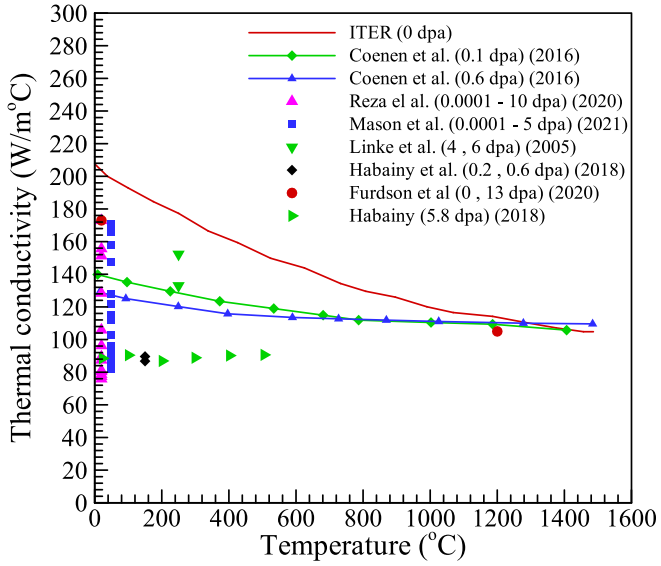

Fig. 7. Thermal conductivity data of W plotted from literature [47,62–64,67–69].

and CuCrZr coolant pipe. The mechanical properties (Young's modulus, Poisson's ratio) for W armour, Cu interlayer and CuCrZr coolant pipe are obtained from the literature [47]. Moreover, parameters such as yield stress and stress–strain data derived from the DD simulation (E, Fig. 1) are implemented in the elasto-plastic model for the mechanical simulation (F, Fig. 1). As the materials within the component experience increasing quantities of irradiation, their properties change. This in turn changes the temperature and stress profiles through the component. However, the rate at which the material properties change, due to neutron irradiation, are a function of these profiles leading to a highly non-linear system. The proposed computational framework allows the component to be assessed at various stages through its lifecycle whilst accounting for this non-linearity in the evolution of its performance.

Lifecycle assessment

The design of the in-vessel components in a tokamak reactor should satisfy certain conditions to withstand the irradiation environment. Prior to the physical testing, the new designs of the in-vessel components must be evaluated by means of 'Structural Design Criteria for In-vessel Components' (SDC-IC) design code to analyse the stress tolerance and assess the failure mode of the components [70,71]. To participate in such testing, numerical results derived from FEA mechanical simulations (G, Fig. 1) are subjected to elastic analysis procedure (EAP) to implement the SDC-IC assessment (G, Fig. 1). SDC-IC design code criteria considers the influence of neutron irradiation of in-vessel components (G, Fig. 1). In a tokamak reactor, the neutron irradiation effects on the in-vessel components are significant, which induce various transmutation products and defects causing undesirable reduction in thermal conductivity, embrittlement and hardening, which affects the actual function of the components. The conventional testing procedures on unirradiated in-vessel components cannot provide insights on the in-service performance. Therefore, it is important to assess the components in both unirradiated and irradiated conditions. In the current study, plastic flow localisation rule (SDC-IC 3121.2) is applied to analyse the lifecycle of in-vessel component for unirradiated and irradiated state (G, Fig. 1). In the plastic flow localisation rule, the total stress (P_L (mechanical) $+Q_L$(secondary)) of the in-vessel component is assessed against the yield stress (S_e), which represents the ductility limits of the material based on Equation (2), where T is the temperature.

$$P_L + Q_L \leq S_e(T, \text{dpa}) \tag{2}$$

The total stress felt by a component comprises of both the primary (mechanical), P_L, and secondary (thermal) stresses, Q_L, that are applied. If the total stress of the material exceeds its ductility, ductile failure occurs. This can be quantified by strength usage and reserve factor, R_f, this being the ratio of S_e and the total stress applied. A value of $R_f < 1$ indicates that ductile failure is likely to occur.

In this study, SDC-IC design structural rules are applied only for the CuCrZr coolant pipe since it serves as the load supporting unit of the monoblock. Moreover, if the pipe structure fails appreciably, the intended function of monoblock component fails to achieve its purpose and consequently affects the heat extraction inside the tokamak reactor. Two operating conditions are studied in the lifecycle assessment:

(1) Normal operating conditions (NOC), consisting of plasma and neutron loads, coolant pressure and temperature.
(2) Stand-by conditions, where the coolant pressure and temperature is maintained across the monoblock, with a coolant temperature of 150 °C.

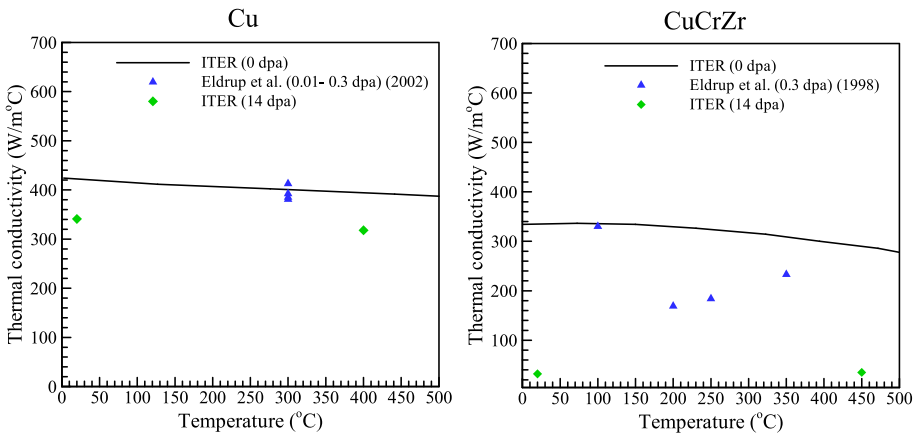

Fig. 8. Thermal conductivity data of Cu interlayer and CuCrZr pipe plotted from literature [47,53,65].

The numerical results obtained from the FEA mechanical and thermal simulations are subjected to plastic flow localisation rule (SDC-IC 3121.2) to perform lifecycle assessment of CuCrZr pipe for unirradiated and irradiated state [71].

Results and discussion

This section reports numerical results for the W monoblock using the multiscale computational framework. The results and associated discussion are presented in subsections for the various simulation stages in the same order as presented in the framework and methodology sections. That is, neutronics, dislocation dynamics, FEA thermal simulation, FEA mechanical simulation and finally lifecycle assessment.

Neutronics simulation

Fig. 9 depicts the scored neutron heating and damage energy for the W monoblock due to the neutron transport from an isotropic fusion energy point source located 15 cm from the monoblock with a Muir energy spectrum (B, Fig. 1). The heating values are tallied onto the OpenMC mesh of the W monoblock discretised along the x, y, and z directions with 200, 100, and 200 points, respectively. It is worth noting that the neutron transport induces heating with the highest value of $6 \times 10^8\ W/m^3$ at the upper portion of the W armour, while at Cu interlayer and CuCrZr cooling tube components, neutron heating values in the range of $1 - 1.2 \times 10^9\ \mathrm{W/m^3}$ are observed. The W armour experiences very low neutron heating values ($<4.0 \times 10^8\ \mathrm{W/m^3}$)at the bottom part of the monoblock. Cu interlayer and CuCrZr cooling channel experiences higher damage energy with respect to W armour as shown in the Fig. 9 b since the threshold energy of Cu and CuCrZr is lower than W.

From the damage energy values, the dpa of the monoblock is computed at the various stages of operation as a function of full power days in fusion energy conditions namely the newly manufactured monoblock installed in the tokamak reactor (day 0) and the degraded state of the monoblock during operation, with day 100 and day 1000 shown in Fig. 10. At day 100, the monoblock experienced a maximum dpa of 3 at the Cu interlayer and CuCrZr pipe while W armour has a dpa value of less than 1.5. However at day 1000, due to the prolonged exposure, the monoblock undergoes higher degradation with a maximum dpa value of 14 in the W armour and 20–40 in the Cu interlayer and CuCrZr cooling channel. It should be noted that error bars are not considered for the calculated neutron heating and damage energy values.

Dislocation dynamics simulation

Based on the FEA thermal simulation results (C, Fig. 1), the temperature distribution across the W armour and Cu interlayer is implemented in the dislocation dynamics (DD) simulation for W and Cu RVEs (D,E, Fig. 1). From the DD analysis, the evolution of the dislocation lines due to the interaction with the neutron irradiation-induced defects and the consequent influence on the yield stress of the W and Cu materials is investigated.

DD simulations are performed for various temperature and dpa dependent irradiation-induced defect densities to study the dislocation line evolution and consequent influence on the yield stress in W and Cu RVE microstructures (Fig. 5, Fig. 6). Fig. 11 shows the evolution of the dislocation configuration for the W RVE embedded with neutron irradiation-induced defects (precipitates and dislocation loops) at a strain rate of $100\ s^{-1}$. This strain rate is chosen based on experience, with

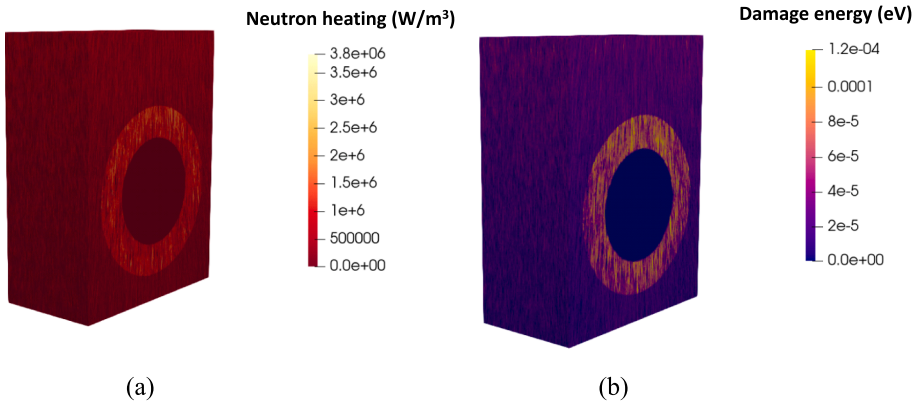

Fig. 9. (a) Neutron heating values and (b) damage energy in the W monoblock.

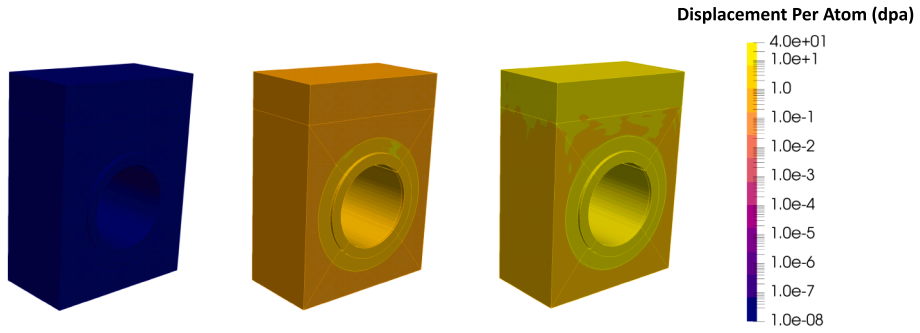

Fig. 10. Dpa of the W monoblock at day 0, day 100, and day 1000 (day 100 and day 1000 refer to full power days).

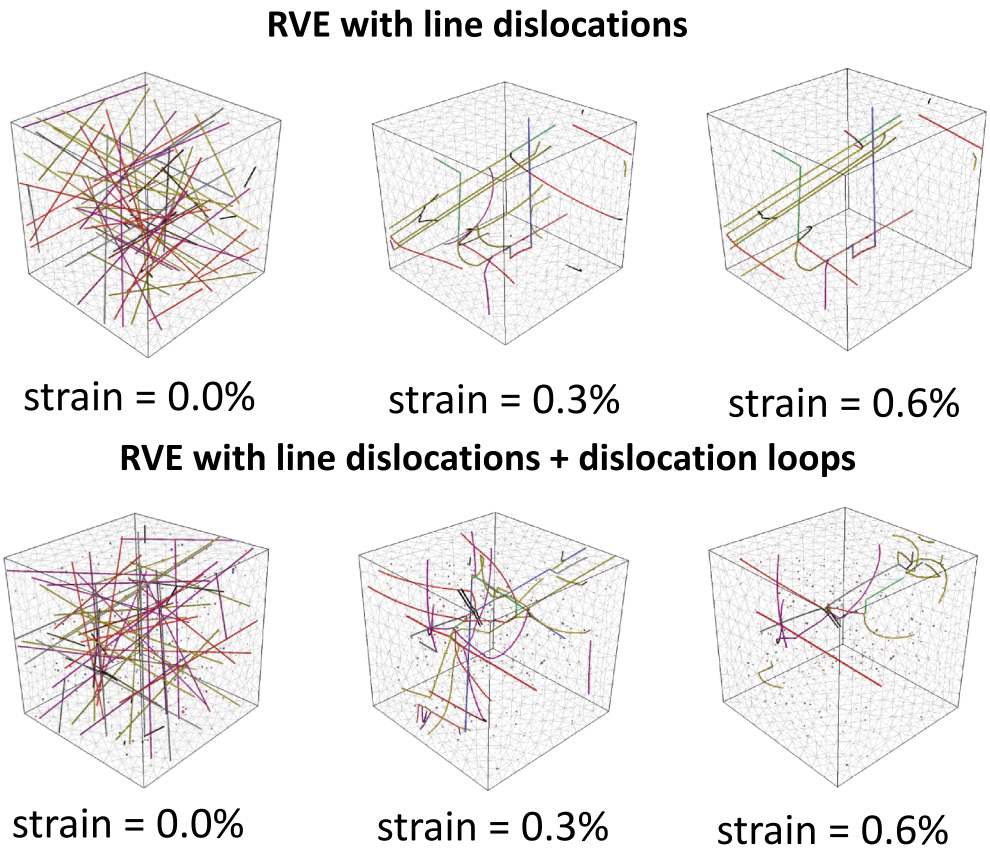

Fig. 11. Dislocation line evolution for the W RVE at different loading stages for a strain rate of 100 s^{-1}.

it providing a compromise between computational expense and accuracy.

Fig. 12 and Fig. 13 depict the yield stress for W and Cu plotted with respect to dpa. Clearly, the yield stress of the W and Cu samples decrease with increasing temperature. The yield stress obtained from the current DD simulations are compared with the literature data [26–28,72–75], highlighting that the increase in yield stress is due to the crystallographic slip resistance of dislocation motion by the defects, which consequently cause the irradiation-induced hardening. In particular, the presence of precipitates and dislocation loops in the W RVE (dpa $>$ 1.6) induces yield stress of high values in comparison with the RVE that included dislocation loops alone (dpa $<$ 1.6). The presence of SFTs and dislocation loops as defects in Cu RVEs increases the yield stress until a dpa of 0.1. At dpa greater than 0.1, the defect cluster density saturates to a constant value and therefore, the yield stress is constant.

FEA thermal simulation

A parametric study is carried out for three different monoblock designs of W armour heights; (a) 23 mm (design 1), (b) 30 mm (design 2) and (c) 32.5 mm (design 3) as shown in Fig. 14. Note that design 2 (Lukenskas et al. [43]) is the design already presented in previous sections of this work. Neutronics simulations (B, Fig. 1) are performed for design 1 and design 3 with the same simulation parameters used for design 2 (section 3.1). Thermal fields and dpa are calculated for both designs from the damage energies and neutron heat loads obtained from the respective neutronics simulation. dpa and other related thermo-mechanical properties and fields are calculated based on damage energies and neutron heat loads values without considering error bars.

FEA thermal simulations (C, Fig. 1) are performed in NOC, which consists of plasma and neutron loads, coolant pressure (5 MPa) and convective cooling. Thermal fields are assessed at day 0, day 100 and day 1000 of the lifecycle stages of the monoblock component. The lifecycle stages are based on the dpa and thermal conductivity, which influences the thermal fields and yield stress, consequently affecting the thermo-mechanical behaviour of the monoblock component. The plasma and neutron load along with the convective cooling results in a high thermal gradient along the monoblock height. Additionally, due to the change in thermal conductivity as a function of dpa and irradiation temperature, variations in the thermal fields are observed at day 0, day 100 and day 1000 for the three designs, which are depicted in Fig. 15 c, Fig. 16 c and Fig. 17 c. Interestingly, at higher dpa and temperature (Fig. 15 a, Fig. 16 a, Fig. 17 a), the lower thermal conductivity values (Fig. 15 b, Fig. 16 b, Fig. 17 b) of the components induce higher temperature gradient across different monoblock designs at day 100 and day 1000. For design 2 and design 3, a peak temperatures of 1400 °C and 2600 °C, respectively (Fig. 16 (c), Fig. 17 (c)) are achieved at day 1000 due to the lower thermal conductivity values and higher thermal gradients. These changes in thermal fields as a function of dpa and irradiation temperature induce variations in the mechanical properties and stress fields of the components at different lifecycle stages during operation. The computational framework developed in this study allows understanding the thermal field evolutions of components in unirradiated and irradiated scenarios, which enables the designer to modify the configuration of the component and down select the appropriate component designs for experimental testing.

It should be noted that in addition to formation of irradiation-induced defects, the hostile conditions in tokamak degrades W due to recrystallization especially above 1350 °C, which results in the alteration of W microstructure [76]. Consequently, the mechanical properties will deteriorate leading to the reduction in lifespan of the component. In the current study, yield stress calculated from the DD simulation does not consider the recrystallization process. A more detailed study can be carried out in the future on the DD model to incorporate the microstructural features of W during a recrystallization process to obtain the yield stress.

FEA mechanical simulation

FEA mechanical simulations (F, Fig. 1) are carried out based on the thermal stress derived from the FEA thermal simulation (C, Fig. 1), coolant pressure and traction boundary conditions at the nodes using Von Mises plastic model for each monoblock design. The dpa and temperature dependent yield stress obtained from the DD simulations (E, Fig. 1) are plotted across the monoblock designs for day 0, day 100, day 1000 based on the dpa and thermal field distribution depicted in Fig. 15 d, Fig. 16 d and Fig. 17 d. In FEA mechanical simulation, linear interpolation is performed in Code_Aster for the yield stress data obtained from the DD simulation for W material (Fig. 12). FEA mechanical simulations are performed on each design to investigate their structural behaviour at different stages of their lifecycle. It should be noted that the centre point of the pipe is kept constant for each sample and, due to the neutron source being applied as a point source, the distance between the sample top surface and the neutron source decreases as the armour thickness increases. That is, design 3 is nearer the source than design 1, which, given the radial type source, results in design 3 receiving a

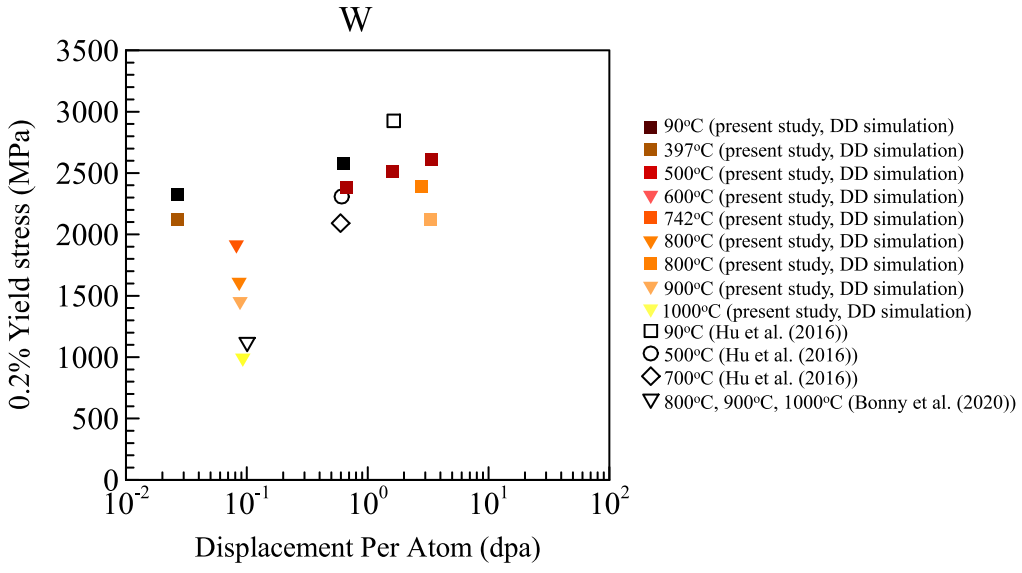

Fig. 12. Yield stress as a function of dpa and temperature for W.

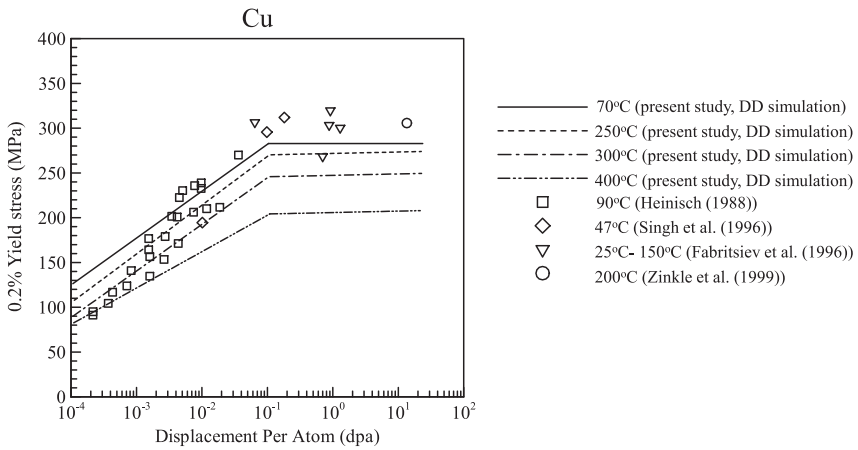

Fig. 13. Yield stress as a function of dpa and temperature for Cu.

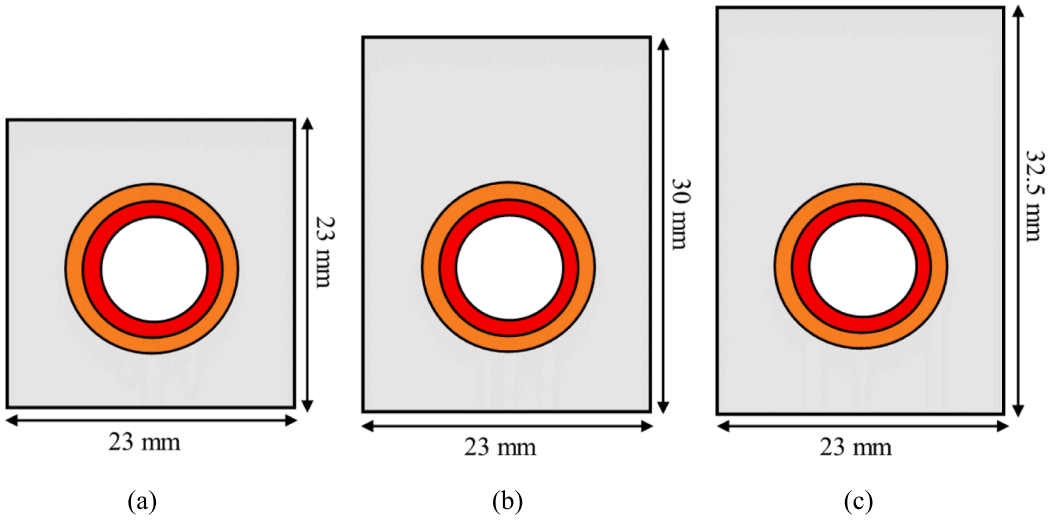

Fig. 14. Monoblock designs (a) design 1 (b) design 2 (c) design 3.

greater count of neutrons. Additionally, increasing the armour thickness increases the distance between the plasma heat source on the top surface and the heat sink on the coolant pipe's inner surface. The resultant impact of the combination of these two mechanisms is that the temperature profile and dpa values, as well as derivative values, vary for each design. Day 0 corresponds to the initial stage of operation of the newly manufactured monoblocks with no defects present in the tokamak reactor. Therefore, at day 0, only temperature dependent yield stress and thermal conductivity is implemented for the FEA. At day 100 and 1000, the neutron irradiation induces damage on the monoblock, which results in spatial and temporal dpa evolution with consequent increase in the yield stress distribution. At higher dpa, the yield stress of the monoblock increases due to the formation of irradiation-induced defects (Fig. 12 - Fig. 13). It should be noted that yield stress at the top regions of the monoblock designs is lower due to the high temperature induced by plasma and neutron heat loads.

It is evident from the Fig. 15(d), Fig. 16 (d) and Fig. 17 (d) that yield stress distribution varies at different lifecycle stages of the components and consequently influences the stress field distribution of the monoblock at day 0, 100 and 1000. The mismatch in the coefficient of thermal expansion induces high Von Mises and principal stress fields at the W armour-Cu interlayer interface and inner surface of CuCrZr pipe shown in Figs. 15-17 (e,f). In addition to the thermal stress, the pressure induced by the fluid flowing through the cooling tube also contributes to the stress at the monoblock. In order to understand the evolution of stress fields at the W-Cu interface and inner surface of CuCrZr, Von Mises and principal stress fields are plotted at the midplane of the monoblock designs as shown in Fig. 18 and Fig. 19. It is evident that the Von Mises and principal stress values for W armour and CuCrZr pipe are higher at day 1000 due to elevated temperature with respect to the day 0 and day 100. Moreover, for design 2 and design 3, the stress fields are lower when compared to design 1, which can be attributed to the increase in length of the W armour (Figs. 15-19).

The monoblock is composed of brittle W and ductile Cu interlayer and CuCrZr pipe. The failure criteria assessment of brittle materials is based on the principal stress values with respect to ultimate strength of the material. If the principal stress values are higher than the ultimate tensile strength, the brittle components undergo failure. In the current study, dose and temperature dependent ultimate strength value of W materials is taken from the work of Garrison et al. [77].

The failure of ductile materials is assessed during the event of plastic deformation, which occurs when the Von Mises stress values are higher than the yield stress values. In the case of Cu interlayer and CuCrZr pipe, the dpa and temperature dependent yield stress values are calculated from the DD simulation (E, Fig. 1) and are implemented to understand its failure assessment based on the Von Mises stress values obtained from the FEA mechanical simulation (F, Fig. 1). Therefore, the failure criteria are assessed in terms of safety factor, which is calculated as the ratio of principal stress to ultimate tensile stress for W and Von Mises stress to yield stress for the Cu interlayer and CuCrZr pipe. The safety factors are

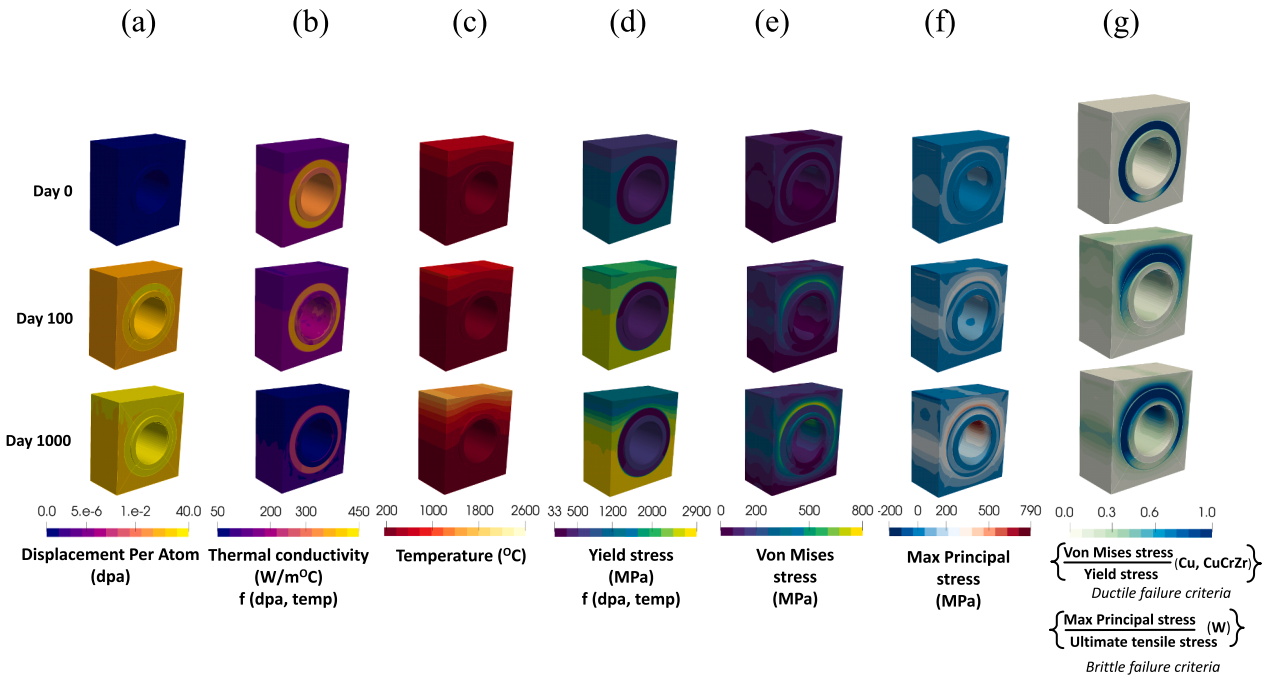

Fig. 15. Plots for W monoblock in NOC at different lifecycle stages (day 0, day 100, day 1000) for design 1 (a) dpa (b) Thermal conductivity (f (dpa, temperature)) (c) Temperature (d) Yield stress (f (dpa, temperature)) (e) Von Mises stress (f) Maximum principal stress (g) Von Mises stress/Yield stress (Cu, CuCrZr) - ductile failure criteria, Max. principal stress/ultimate tensile stress (W) - brittle failure criteria (day 100 and day 1000 refer to full power days).

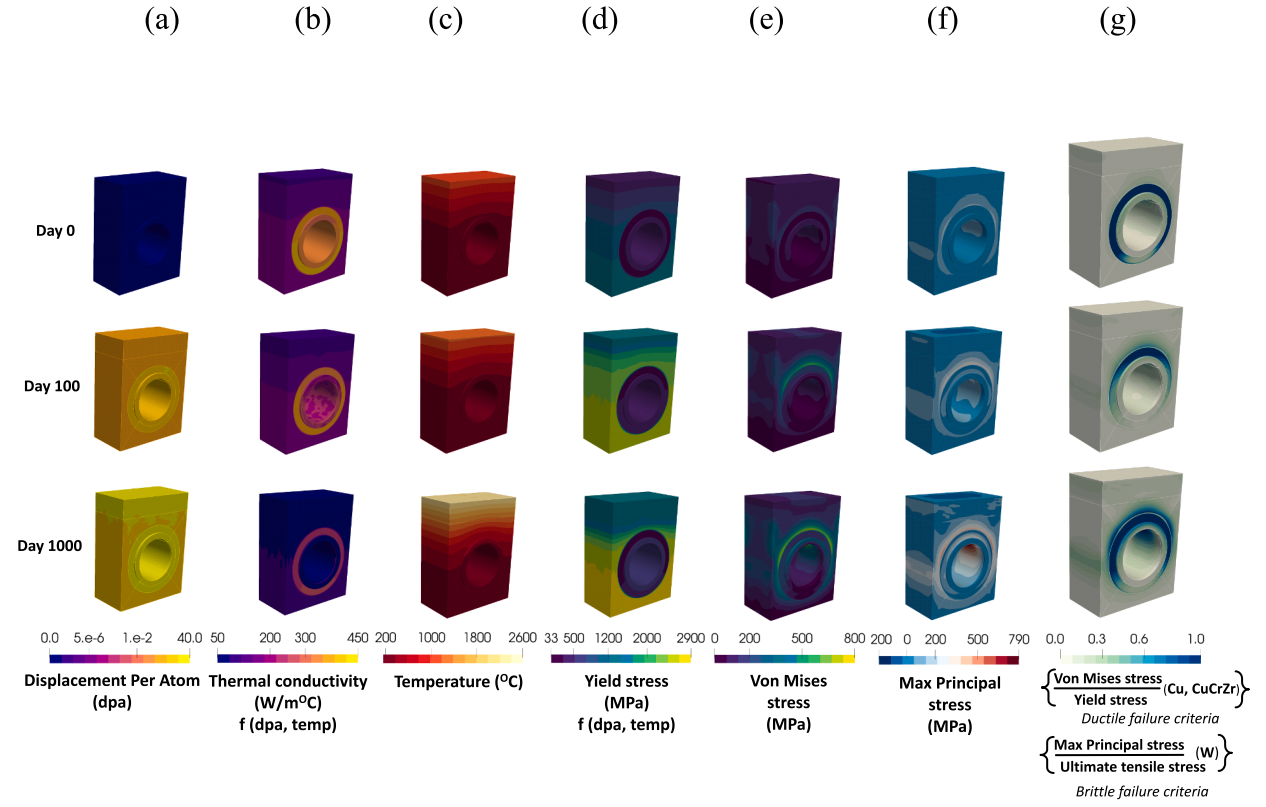

Fig. 16. Plots for W monoblock in NOC at different lifecycle stages (day 0, day 100, day 1000) for design 2 (a) dpa (b) Thermal conductivity (f (dpa, temperature)) (c) Temperature (d) Yield stress (f (dpa, temperature)) (e) Von Mises stress (f) Maximum principal stress (g) Von Mises stress/Yield stress (Cu, CuCrZr) - ductile failure criteria, Max. principal stress/ultimate tensile stress (W) - brittle failure criteria (day 100 and day 1000 refer to full power days).

shown in Fig. 15 (g), Fig. 16 (g) and Fig. 17 (g) for the three monoblock designs. Safety factor of greater than 1 indicates that the component has undergone failure while safety factor values greater than 0.75 and less than 1 represent the material is at the risk of failure. The material is operating in safe limits if the safety factor values are less than 0.75. The safety factor values of W armour are less than 0.5, which shows that the

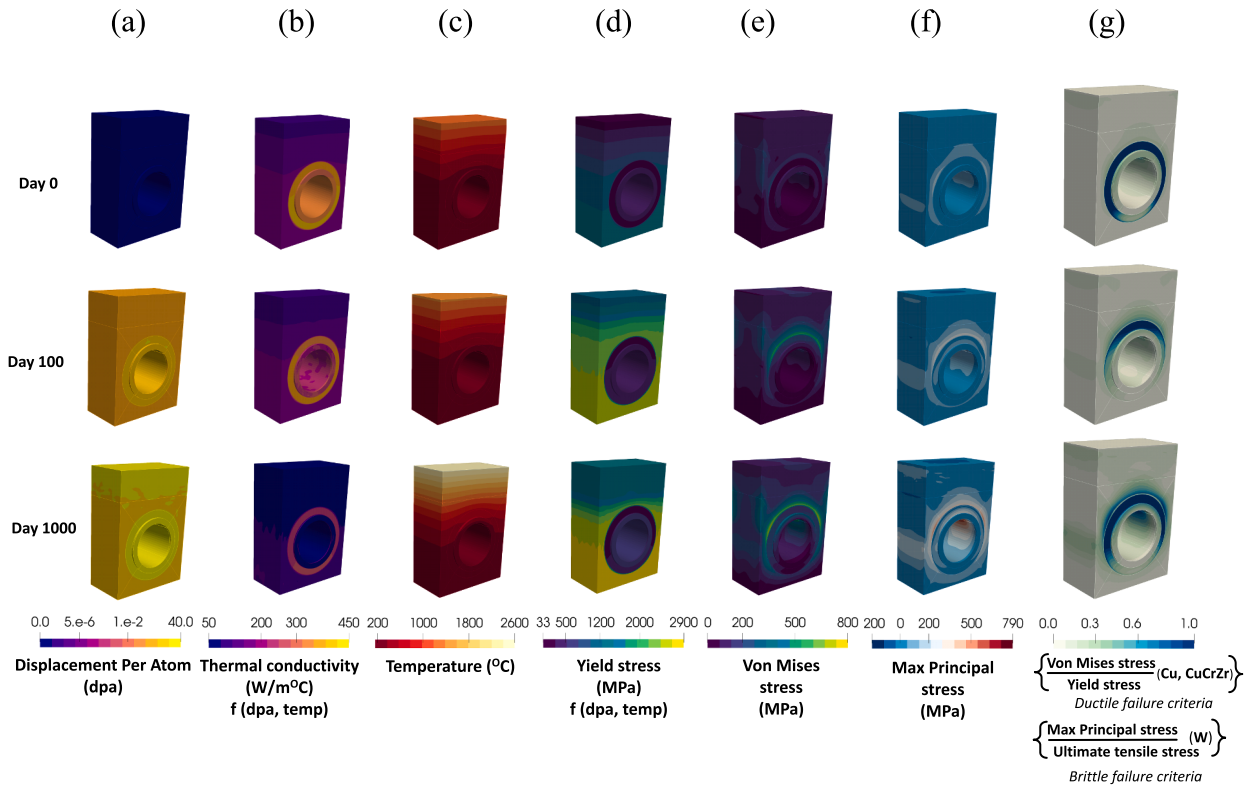

Fig. 17. Plots for W monoblock in NOC at different lifecycle stages (day 0, day 100, day 1000) for design 3 (a) dpa (b) Thermal conductivity (f (dpa, temperature)) (c) Temperature (d) Yield stress (f (dpa, temperature)) (e) Von Mises stress (f) Maximum principal stress (g) Von Mises stress/Yield stress (Cu, CuCrZr) - ductile failure criteria, Max. principal stress/ultimate tensile stress (W) - brittle failure criteria (day 100 and day 1000 refer to full power days).

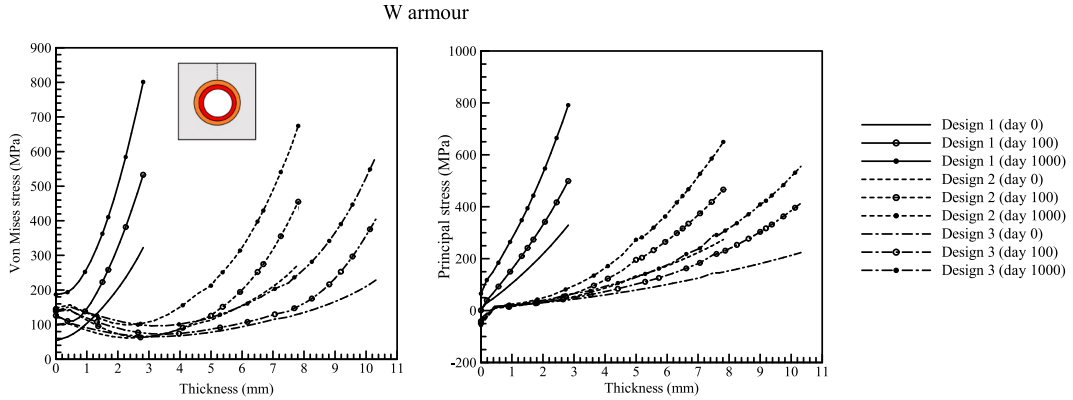

Fig. 18. Von Mises stress (left) and maximum principal stress (right) plotted along the dotted lines of W armour at the midplane of the monoblock for design 1, design 2 and design 3.

W armour is operating within safe limits in both unirradiated and irradiated regime for different monoblock designs. In the case of CuCrZr pipe, the stress values are in the safety range for day 0 (unirradiated) and day 100 (irradiated) since the safety factor is less than 0.75 for each design. However, for day 1000, the safety factor of the pipe is greater than 0.75 indicating that it is at risk of failure. This type of failure assessment is used as a preliminary step to understand whether the material has already undergone failure based on the Von Mises and principal stress fields obtained from the FEA mechanical simulations in unirradiated (day 0) and irradiated (day 100, day 1000) conditions.

During the operation of tokamak, only few monoblocks (~ 2), in the Plasma-Facing-Unit (PFU) located near the strike points, will be subjected to plasma induced high heat flux and neutron loads. However, the remaining monoblocks will maintain a temperature close to the coolant temperature, which are only exposed to neutron loads. To understand this scenario, we performed FEA simulations for design 1 at day 100 considering NOC without plasma loads (only neutron loads). The results are depicted in Fig. 20 and a comparison is made against NOC.

It is interesting to note that thermal and stress fields in NOC are higher than the case with NOC without plasma loads. In particular, there are no possibilities of failure of monoblock subjected to NOC without plasma loads.

Lifecycle assessment

In this section, the results derived from the FEA simulations for CuCrZr pipe are implemented for SDC-IC assessment (G) integrated into the computational framework. Plastic flow localisation rules are

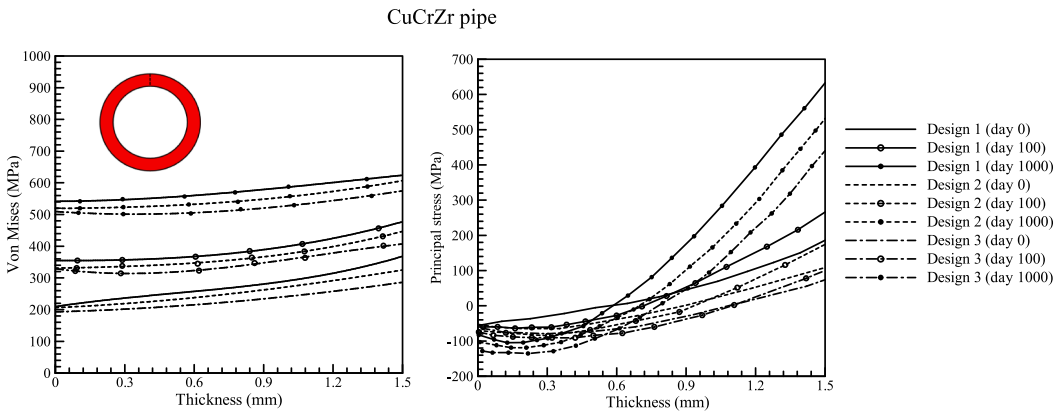

Fig. 19. Von Mises stress (left) and maximum principal stress (right) plotted along the dotted lines of CuCrZr pipe at the midplane of the monoblock for design 1, design 2 and design 3.

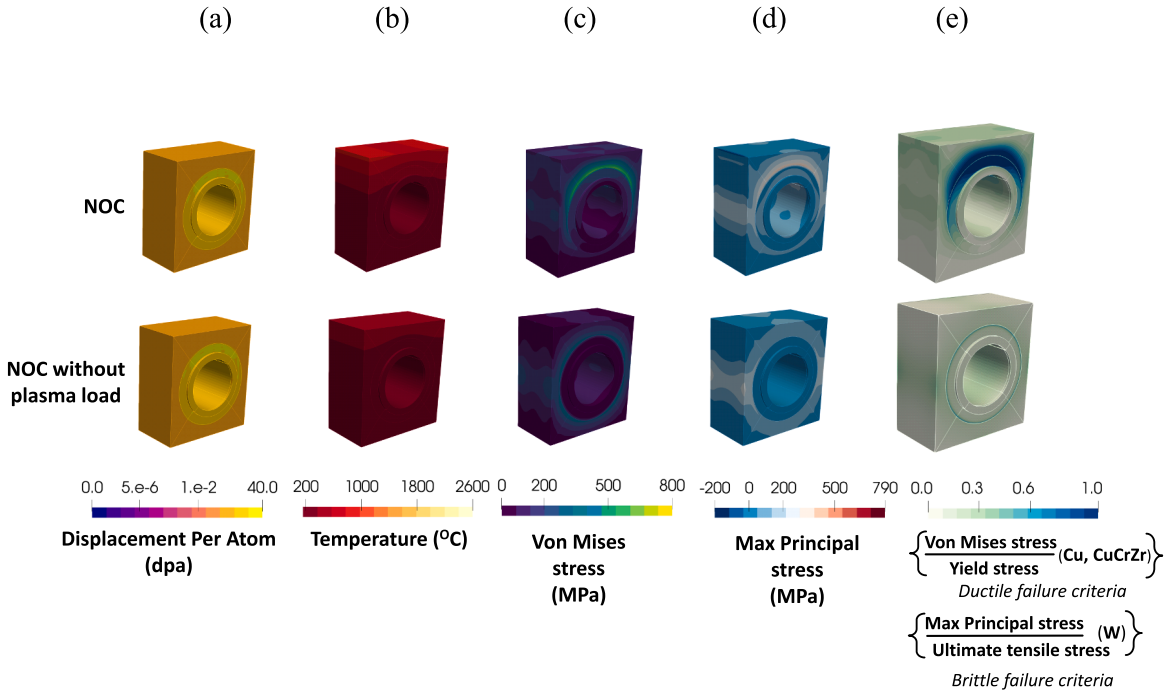

Fig. 20. Plots for W monoblock at day 100 considering NOC (top) and NOC without plasma load (bottom) for design 1 (a) dpa (b) Temperature (c) Von Mises stress (d) Maximum principal stress (e) Von Mises stress/Yield stress (Cu, CuCrZr) - ductile failure criteria, Max. principal stress/ultimate tensile stress (W) - brittle failure criteria.

employed in NOC and stand-by conditions. As depicted in previous section, the stress fields across the monoblock components varies for unirradiated (day 0) and irradiated case (day 100, day 1000). To assess whether the stress fields exceed the local strength of the material, it is necessary to investigate the locations of high stress area, which has the highest failure probability. Therefore, stress linearisation is performed at regions of maximum temperature, minimum temperature, and maximum stress in the CuCrZr pipe. In the case of stand-by conditions, stress linearisation is performed only for maximum stress region since the temperature is uniform across the pipe. Fig. 21 shows the Von Mises stress distribution of CuCrZr pipe in NOC and stand-by conditions. The SDC-IC assessment for plastic flow localisation rule is expressed in terms of strength usage of the materials and R_f (inverse of the strength usage of the material). Von Mises stress (total stress ($P_L + Q_L$)) derived from FEA mechanical simulation is employed to calculate the strength usage based on the yield stress of the material in NOC and standby conditions. The strength usage and R_f are reported in Fig. 22 and Tables 3-5 for unirradiated (day 0) and irradiated (day 100, day 1000) cases.

For the unirradiated case (day 0), in NOC, the stress field maximum (260 MPa) is higher than the stand-by conditions (160 MPa). A similar trend is observed for the irradiated case with higher values of stress in NOC when compared to stand-by conditions as reported in the Tables 3-5. The temperature and stress fields at locations of maximum stress, maximum temperature and minimum temperature are reported in Tables 3–5 for NOC and stand-by conditions for unirradiated and irradiated case. For each design in the unirradiated case the strength usage and R_f of CuCrZr pipe are within the safe limits and no ductile failure occurs. In particular, the ductile failure occurs only for design 1 for day 1000 in which the strength usage and R_f surpasses the safe limits. The current study has only incorporated the variation of W armour to assess the performance of various monoblock designs and its failure probabilities using plastic flow localisation rule. However, the computational framework employed in this study enables other in-vessel components, such as breeder blanket, to be investigated to evaluate its failure

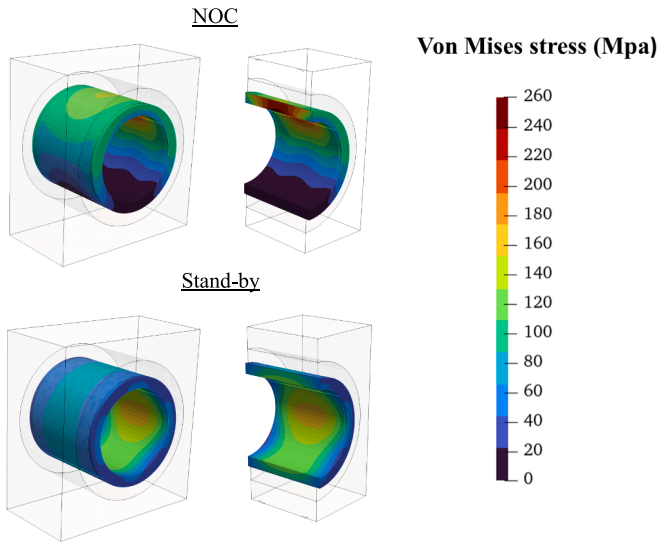

Fig. 21. Von Mises stress of CuCrZr pipe in NOC and stand-by condition.

probability.

Conclusions

Currently, there is insufficient fusion relevant experimental data available, which characterises the change in material properties due to neutron damage. This is a significant challenge to the development of fusion component designs that are optimised for their expected life cycle. This work presents a multiscale numerical framework to address this challenge. It facilitates investigating the influence of neutron irradiation-induced defects on the mechanical properties of tokamak in-vessel components. The neutron induced changes are considered spatially, depending on the geometry of the component and its location within the tokamak, and temporally by considering various stages of their operational lifecycle.

With respect to the previous studies on the multiscale property assessments, a core tenet of the current computational framework is parameterisation of the geometries and simulation parameters. This facilitates accelerated investigations into how the thermo-mechanical performance of various design concepts changes over their lifecycles. Because it is also modular, there is flexibility to replace stages of the workflow with improved theoretical models, simulations, or experimental data when they become available and automatically recalculate the consequential steps for comparison. Thus, further work is essential to validate the multiscale computational framework against the experimental data as and when experimental and other data are produced. As a way of rapidly generating data across a multi-dimensional parameter space, this could be used as an automated optimisation tool using conventional algorithms or more state-of-the-art machine learning methods. The hope is that this computational framework makes a significant contribution to the fusion research community's efforts in designing the first generation of fusion energy powerplants.

CRediT authorship contribution statement

Salahudeen Mohamed: Writing – review & editing, Writing – original draft, Methodology, Investigation, Formal analysis, Conceptualization. **Giacomo Po:** Writing – review & editing, Resources, Investigation. **Rhydian Lewis:** Writing – review & editing, Software, Resources. **Perumal Nithiarasu:** Writing – review & editing, Resources.

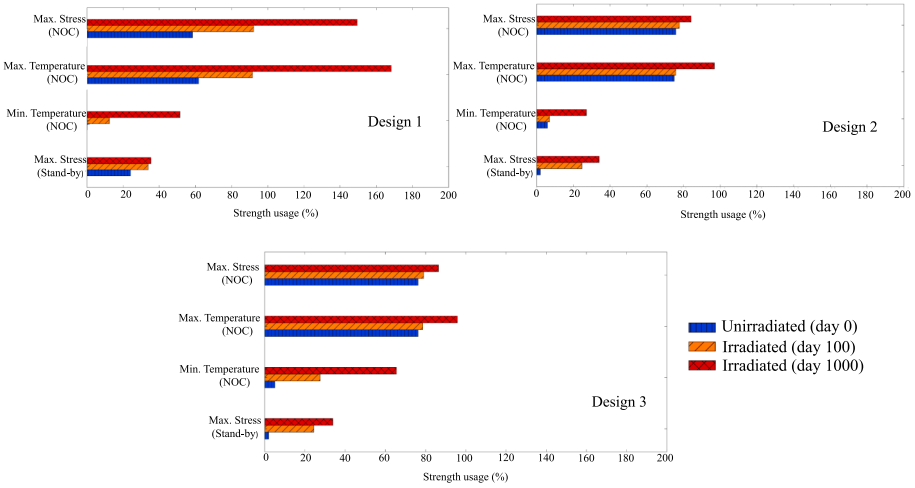

Fig. 22. Strength usage of CuCrZr pipe for design 1, design 2, design 3 for unirradiated (day 0) and irradiated (day 100, day 1000) conditions (day 100, day 1000 refer to full power days).

Table 3
R_f of CuCrZr pipe in unirradiated and irradiated conditions for design 1.

Operating condition	Temperature (°C)			Total stress, $P_L + Q_L$ (MPa)			R_f		
	Un-irrad (day 0)	Irrad. (day 100)	Irrad. (day 1000)	Un-irrad (day 0)	Irrad. (day 100)	Irrad. (day 1000)	Irrad. (day 0)	Irrad. (day 100)	Irrad. (day 1000)
Max. Stress (NOC)	282.81	400.69	221.00	256.48	341.79	525.30	1.67	1.10	0.60
Max. Temp (NOC)	345.00	410.00	462.00	133.00	273.00	354.90	1.61	1.08	0.58
Min. Temp (NOC)	158.06	274.00	161.00	10.90	143.68	85.00	55.0	7.63	1.92
Max. Stress (Stand-by)	150.00	150.00	150.00	152.62	160.00	163.00	4.03	2.90	2.73

Table 4
R_f of CuCrZr pipe in unirradiated and irradiated conditions for design 2.

Operating condition	Temperature (°C)			Total stress, $P_L + Q_L$ (MPa)			R_f		
	Un-irrad (day 0)	Irrad. (day 100)	Irrad. (day 1000)	Un-irrad (day 0)	Irrad. (day 100)	Irrad. (day 1000)	Irrad. (day 0)	Irrad. (day 100)	Irrad. (day 1000)
Max. Stress (NOC)	284.06	389.33	425.52	286.60	331.45	527.08	1.30	1.28	1.18
Max. Temp (NOC)	347.91	398.47	512.00	121.29	263.42	355.39	1.34	1.08	1.02
Min. Temp (NOC)	273.38	157.64	159.49	88.41	51.26	61.92	15.0	1.31	3.57
Max. Stress (Stand-by)	150.00	150.00	150.00	151.35	156.38	159.03	5.00	4.00	2.85

Table 5
R_f of CuCrZr pipe in unirradiated and irradiated conditions for design 3.

Operating condition	Temperature (°C)			Total stress, $P_L + Q_L$ (MPa)			R_f		
	Un-irrad (day 0)	Irrad. (day 100)	Irrad. (day 1000)	Un-irrad (day 0)	Irrad. (day 100)	Irrad. (day 1000)	Irrad. (day 0)	Irrad. (day 100)	Irrad. (day 1000)
Max. Stress (NOC)	282.22	380.80	459.33	298.74	325.87	518.34	1.28	1.25	1.15
Max. Temp (NOC)	345.18	388.07	553.06	117.89	267.05	356.79	1.29	1.26	1.04
Min. Temp (NOC)	271.68	156.78	239.85	104.44	38.46	226.09	17.0	3.63	1.52
Max. Stress (Stand-by)	150.00	150.00	150.00	151.35	156.38	159.03	6.05	4.05	2.90

Declaration of competing interest

The authors declare that they have no known competing financial interests or personal relationships that could have appeared to influence the work reported in this paper.

Data availability

In order to reproduce the numerical results reported in the current paper, the relevant numerical codes and tutorials are provided in the Gitlab repository. -
https://gitlab.com/ibsim/virtuallab-
https://virtuallab.readthedocs.io/en/docs/examples/Irradiation_damage.html

Acknowledgements

This work has been carried out within the framework of the EUROfusion Consortium, funded by the European Union via the Euratom Research and Training Programme (Grant Agreement No 101052200 - EUROfusion). It has also been part funded by EPSRC [grant number EP/R012091/1]. Views and opinions expressed are however those of the author(s) only and do not necessarily reflect those of the European Union or the European Commission. Neither the European Union nor the European Commission can be held responsible for them. We acknowledge the support of the Supercomputing Wales and AccelerateAI projects, which are part-funded by the European Regional Development Fund (ERDF) via Welsh Government.

References

[1] S.L. Dudarev, J.-L. Boutard, R. Lässer, M.J. Caturla, P.M. Derlet, M. Fivel, C.-C. Fu, M.Y. Lavrentiev, L. Malerba, M. Mrovec, D. Nguyen-Manh, K. Nordlund, M. Perlado, R. Schäublin, H. Van Swygenhoven, D. Terentyev, J. Wallenius, D. Weygand, F. Willaime, The EU programme for modelling radiation effects in fusion reactor materials: An overview of recent advances and future goals, J. Nucl. Mater. 386–388 (2009) 1–7, https://doi.org/10.1016/j.jnucmat.2008.12.301.

[2] G. Federici, W. Biel, M.R. Gilbert, R. Kemp, N. Taylor, R. Wenninger, European DEMO design strategy and consequences for materials, Nucl. Fusion 57 (2017) 092002, https://doi.org/10.1088/1741-4326/57/9/092002.

[3] C.h. Linsmeier, M. Rieth, J. Aktaa, T. Chikada, A. Hoffmann, J. Hoffmann, A. Houben, H. Kurishita, X. Jin, M. Li, A. Litnovsky, S. Matsuo, A. von Müller, V. Nikolic, T. Palacios, R. Pippan, D. Qu, J. Reiser, J. Riesch, T. Shikama, R. Stieglitz, T. Weber, S. Wurster, J.-H. You, Z. Zhou, Development of advanced high heat flux and plasma-facing materials, Nucl. Fusion 57 (2017) 092007, https://doi.org/10.1088/1741-4326/aa6f71.

[4] A. Lehtinen, L. Laurson, F. Granberg, K. Nordlund, M.J. Alava, Effects of precipitates and dislocation loops on the yield stress of irradiated iron, Sci. Rep. 8 (2018) 6914, https://doi.org/10.1038/s41598-018-25285-z.

[5] C. Dethloff, E. Gaganidze, J. Aktaa, Microstructural defects in EUROFER 97 after different neutron irradiation conditions, Nucl. Mater. Energy 9 (2016) 471–475, https://doi.org/10.1016/j.nme.2016.05.009.

[6] C. Obitz, J. Öijerholm, S. Wikman, E. Bratu, Erosion corrosion of CuCrZr specimens exposed for simulated ITER operational conditions, Nucl. Mater. Energy 9 (2016) 261–266, https://doi.org/10.1016/j.nme.2016.05.001.

[7] A. Herrmann, H. Greuner, M. Balden, H. Bolt, Design and evaluation of an optimized W/Cu interlayer for W monoblock components, Fusion Eng. Des. 86 (2011) 27–32, https://doi.org/10.1016/j.fusengdes.2010.07.018.

[8] M.R. Gilbert, S.L. Dudarev, D. Nguyen-Manh, S. Zheng, L.W. Packer, J.-C. Sublet, Neutron-induced dpa, transmutations, gas production, and helium embrittlement of fusion materials, J. Nucl. Mater. 442 (2013) S755–S760, https://doi.org/10.1016/j.jnucmat.2013.03.085.

[9] J. Linke, J. Du, T. Loewenhoff, G. Pintsuk, B. Spilker, I. Steudel, M. Wirtz, Challenges for plasma-facing components in nuclear fusion, Matter Radiat. Extrem. 4 (2019) 056201, https://doi.org/10.1063/1.5090100.

[10] C. Yin, D. Terentyev, S. Van Dyck, A. Stankovskiy, R.H. Petrov, T. Pardoen, Effect of high-temperature neutron irradiation on fracture toughness of ITER-specification tungsten, Phys. Scr. T171 (2020) 014052, https://doi.org/10.1088/1402-4896/ab54d7.

[11] P. Gavila, B. Riccardi, S. Constans, J.L. Jouvelot, I.B. Vastra, M. Missirlian, M. Richou, High heat flux testing of mock-ups for a full tungsten ITER divertor, Fusion Eng. Des. 86 (2011) 1652–1655, https://doi.org/10.1016/j.fusengdes.2011.02.012.

[12] M. Dürrschnabel, M. Klimenkov, U. Jäntsch, M. Rieth, H.C. Schneider, D. Terentyev, New insights into microstructure of neutron-irradiated tungsten, Sci. Rep. 11 (2021) 7572, https://doi.org/10.1038/s41598-021-86746-6.

[13] S. Das, Recent advances in characterising irradiation damage in tungsten for fusion power, SN Appl. Sci. 1 (2019) 1614, https://doi.org/10.1007/s42452-019-1591-0.

[14] M.R. Gilbert, J. Marian, J.-C. Sublet, Energy spectra of primary knock-on atoms under neutron irradiation, J. Nucl. Mater. 467 (2015) 121–134, https://doi.org/10.1016/j.jnucmat.2015.09.023.

[15] A. Khan, R. Elliman, C. Corr, J.J.H. Lim, A. Forrest, P. Mummery, L.M. Evans, Effect of rhenium irradiations on the mechanical properties of tungsten for nuclear fusion applications, J. Nucl. Mater. 477 (2016) 42–49, https://doi.org/10.1016/j.jnucmat.2016.05.003.

[16] C.N. Taylor, M. Shimada, J.M. Watkins, X. Hu, Y. Oya, Neutron irradiated tungsten bulk defect characterization by positron annihilation spectroscopy, Nucl. Mater. Energy 26 (2021) 100936, https://doi.org/10.1016/j.nme.2021.100936.

[17] C. Chang, D. Terentyev, A. Zinovev, W. Van Renterghem, C. Yin, P. Verleysen, T. Pardoen, M. Vilémová, J. Matějíček, Irradiation-induced hardening in fusion relevant tungsten grades with different initial microstructures, Phys. Scr. 96 (2021) 124021, https://doi.org/10.1088/1402-4896/ac2181.

[18] E. Martinez, J. Marian, A. Arsenlis, M. Victoria, J.M. Perlado, A dislocation dynamics study of the strength of stacking fault tetrahedra. Part I: interactions with screw dislocations, Philos. Mag. 88 (2008) 809–840, https://doi.org/10.1080/14786430801986662.

[19] Y. Cui, N. Ghoniem, G. Po, Plasticity of irradiated materials at the nano and micro-scales, J. Nucl. Mater. 546 (2021) 152746, https://doi.org/10.1016/j.jnucmat.2020.152746.

[21] Y. Cui, G. Po, N.M. Ghoniem, A coupled dislocation dynamics-continuum barrier field model with application to irradiated materials, Int. J. Plast. 104 (2018) 54–67, https://doi.org/10.1016/j.ijplas.2018.01.015.

[22] J. Marian, S. Fitzgerald, G. Po, Discrete Dislocation Dynamics Simulations of Irradiation Hardening in Nuclear Materials, in: W. Andreoni, S. Yip (Eds.), Handb. Mater. Model., Springer International Publishing, Cham, 2020: pp. 2243–2271. 10.1007/978-3-319-44680-6_121.

[23] M. Fukuda, A. Hasegawa, S. Nogami, K. Yabuuchi, Microstructure development of dispersion-strengthened tungsten due to neutron irradiation, J. Nucl. Mater. 449 (2014) 213–218, https://doi.org/10.1016/j.jnucmat.2013.10.012.

[24] T. Miyazawa, L.M. Garrison, J.W. Geringer, M. Fukuda, Y. Katoh, T. Hinoki, A. Hasegawa, Neutron irradiation effects on the mechanical properties of powder metallurgical processed tungsten alloys, J. Nucl. Mater. 529 (2020) 151910, https://doi.org/10.1016/j.jnucmat.2019.151910.

[25] E. Gaganidze, A. Chauhan, H.-C. Schneider, D. Terentyev, G. Borghmans, J. Aktaa, Fracture-mechanical properties of neutron irradiated ITER specification tungsten, J. Nucl. Mater. 547 (2021) 152761, https://doi.org/10.1016/j.jnucmat.2020.152761.

[26] G. Bonny, M.J. Konstantinovic, A. Bakaeva, C. Yin, N. Castin, K. Mergia, V. Chatzikos, S. Dellis, T. Khvan, A. Bakaev, A. Dubinko, D. Terentyev, Trends in vacancy distribution and hardness of high temperature neutron irradiated single crystal tungsten, Acta Mater. 198 (2020) 1–9, https://doi.org/10.1016/j.actamat.2020.07.047.

[27] X. Hu, T. Koyanagi, M. Fukuda, N.A.P.K. Kumar, L.L. Snead, B.D. Wirth, Y. Katoh, Irradiation hardening of pure tungsten exposed to neutron irradiation, J. Nucl. Mater. 480 (2016) 235–243, https://doi.org/10.1016/j.jnucmat.2016.08.024.

[28] D. Terentyev, C.-C. Chang, C. Yin, A. Zinovev, X.-F. He, Neutron irradiation effects on mechanical properties of ITER specification tungsten, Tungsten 3 (2021) 415–433, https://doi.org/10.1007/s42864-021-00105-6.

[29] A.A. Kohnert, B.D. Wirth, L. Capolungo, Modeling microstructural evolution in irradiated materials with cluster dynamics methods: A review, Comput. Mater. Sci. 149 (2018) 442–459, https://doi.org/10.1016/j.commatsci.2018.02.049.

[30] N. Kvashin, P.L. García-Müller, N. Anento, A. Serra, Atomic processes of shear-coupled migration in 112 twins and vicinal grain boundaries in bcc-Fe, Phys. Rev. Mater. 4 (2020) 073604, https://doi.org/10.1103/PhysRevMaterials.4.073604.

[31] D. Li, H. Zbib, X. Sun, M. Khaleel, Predicting plastic flow and irradiation hardening of iron single crystal with mechanism-based continuum dislocation dynamics, Int. J. Plast. 52 (2014) 3–17, https://doi.org/10.1016/j.ijplas.2013.01.015.

[32] B.D. Wirth, M.J. Caturla, T. Diaz de la Rubia, T. Khraishi, H. Zbib, Mechanical property degradation in irradiated materials: A multiscale modeling approach, Nucl. Instrum. Methods Phys. Res. Sect. B Beam Interact. Mater. At. 180 (2001) 23–31, https://doi.org/10.1016/S0168-583X(01)00392-5.

[33] S.L. Dudarev, D.R. Mason, E. Tarleton, P.-W. Ma, A.E. Sand, A multi-scale model for stresses, strains and swelling of reactor components under irradiation, Nucl. Fusion 58 (2018) 126002, https://doi.org/10.1088/1741-4326/aadb48.

[34] M.A. Oude Vrielink, J.A.W. van Dommelen, M.G.D. Geers, Multi-scale fracture probability analysis of tungsten monoblocks under fusion conditions, Nucl. Mater. Energy 28 (2021) 101032, https://doi.org/10.1016/j.nme.2021.101032.

[35] Y. Wang, X. Sun, J. Zhao, A mechanism-based quantitative multi-scale framework for investigating irradiation hardening of tungsten at low temperature, Mater. Sci. Eng. A 774 (2020) 138941, https://doi.org/10.1016/j.msea.2020.138941.

[36] P.K. Romano, N.E. Horelik, B.R. Herman, A.G. Nelson, B. Forget, K. Smith, OpenMC: A state-of-the-art Monte Carlo code for research and development, Ann. Nucl. Energy 82 (2015) 90–97, https://doi.org/10.1016/j.anucene.2014.07.048.

[37] K. Zhang, A.C. Muñoz, V.H. Sanchez-Espinoza, Development and verification of the coupled thermal–hydraulic code – TRACE/SCF based on the ICoCo interface and the SALOME platform, Ann. Nucl. Energy 155 (2021) 108169, https://doi.org/10.1016/j.anucene.2021.108169.

[38] J. Shimwell, R. Delaporte-Mathurin, J.-C. Jaboulay, J. Aubert, C. Richardson, C. Bowman, A. Davis, A. Lahiff, J. Bernardi, S. Yasin, X. Tang, Multiphysics analysis with CAD-based parametric breeding blanket creation for rapid design iteration, Nucl. Fusion 59 (2019) 046019, https://doi.org/10.1088/1741-4326/ab0016.

[39] G. Po, Y. Cui, D. Rivera, D. Cereceda, T.D. Swinburne, J. Marian, N. Ghoniem, A phenomenological dislocation mobility law for bcc metals, Acta Mater. 119 (2016) 123–135, https://doi.org/10.1016/j.actamat.2016.08.016.

[40] C.D. Hansen, C.R. Johnson, The visualization handbook, Elsevier-Butterworth Heinemann, Amsterdam Boston, 2005.

[41] T. Schwarz-Selinger, A critical review of experiments on deuterium retention in displacement-damaged tungsten as function of damaging dose, Mater. Res. Express 10 (2023) 102002, https://doi.org/10.1088/2053-1591/acfdf8.

[42] R. Delaporte-Mathurin, E.A. Hodille, J. Mougenot, Y. Charles, C. Grisolia, Finite element analysis of hydrogen retention in ITER plasma facing components using FESTIM, Nucl. Mater. Energy 21 (2019) 100709, https://doi.org/10.1016/j.nme.2019.100709.

[43] A. Lukenskas, T.R. Barrett, M. Fursdon, F. Domptail, F. Schoofs, H. Greuner, G. Dose, S. Roccella, E. Visca, F. Gallay, M. Richou, J.-H. You, High heat flux test results for a thermal break DEMO divertor target and subsequent design and manufacture development, Fusion Eng. Des. 146 (2019) 1657–1660, https://doi.org/10.1016/j.fusengdes.2019.03.010.

[44] M. Fursdon, T. Barrett, F. Domptail, L.M. Evans, N. Luzginova, N.H. Greuner, J.-H. You, M. Li, M. Richou, F. Gallay, E. Visca, The development and testing of the thermal break divertor monoblock target design delivering 20 MW m $^{-2}$ heat load capability, Phys. Scr. T170 (2017) 014042, https://doi.org/10.1088/1402-4896/aa8c8e.

[45] K. Nordlund, S.J. Zinkle, A.E. Sand, F. Granberg, R.S. Averback, R. Stoller, T. Suzudo, L. Malerba, F. Banhart, W.J. Weber, F. Willaime, S.L. Dudarev, D. Simeone, Improving atomic displacement and replacement calculations with physically realistic damage models, Nat. Commun. 9 (2018) 1084, https://doi.org/10.1038/s41467-018-03415-5.

[46] P.P.H. Wilson, T.J. Tautges, J.A. Kraftcheck, B.M. Smith, D.L. Henderson, Acceleration techniques for the direct use of CAD-based geometry in fusion neutronics analysis, Fusion Eng. Des. 85 (2010) 1759–1765, https://doi.org/10.1016/j.fusengdes.2010.05.030.

[47] V. Barabash, "Appendix A, Materials design limit data." 222RLN, ITER (2013)., n.d.

[48] M.J. Norgett, M.T. Robinson, I.M. Torrens, A proposed method of calculating displacement dose rates, Nucl. Eng. Des. 33 (1975) 50–54, https://doi.org/10.1016/0029-5493(75)90035-7.

[49] P.-W. Ma, D.R. Mason, S.L. Dudarev, Multiscale analysis of dislocation loops and voids in tungsten, Phys. Rev. Mater. 4 (2020) 103609, https://doi.org/10.1103/PhysRevMaterials.4.103609.

[50] T. Koyanagi, N.A.P.K. Kumar, T. Hwang, L.M. Garrison, X. Hu, L.L. Snead, Y. Katoh, Microstructural evolution of pure tungsten neutron irradiated with a mixed energy spectrum, J. Nucl. Mater. 490 (2017) 66–74, https://doi.org/10.1016/j.jnucmat.2017.04.010.

[51] T. Mura, Micromechanics of defects in solids, Springer Netherlands, Dordrecht, 1987. 10.1007/978-94-009-3489-4.

[52] N. Kishore, B. Sudheer Kumar, K.N.V.K. Manoj, D. Balamurugan, S. Sriram, Mechanical properties of tungsten-rhenium, lanthanum and copper doped tungsten-rhenium nanostructures – A DFT study, Mater. Sci. Eng. B 278 (2022) 115626, https://doi.org/10.1016/j.mseb.2022.115626.

[53] M. Eldrup, B.N. Singh, S.J. Zinkle, T.S. Byun, K. Farrell, Dose dependence of defect accumulation in neutron irradiated copper and iron, J. Nucl. Mater. 307–311 (2002) 912–917, https://doi.org/10.1016/S0022-3115(02)01160-1.

[54] D.J. Edwards, B.N. Singh, J.B. Bilde-Sørensen, Initiation and propagation of cleared channels in neutron-irradiated pure copper and a precipitation hardened CuCrZr alloy, J. Nucl. Mater. 342 (2005) 164–178, https://doi.org/10.1016/j.jnucmat.2005.04.001.

[55] S.J. Zinkle, K. Farrell, Void swelling and defect cluster formation in reactor-irradiated copper, J. Nucl. Mater. 168 (1989) 262–267, https://doi.org/10.1016/0022-3115(89)90591-6.

[56] S.J. Zinkle, K. Farrell, H. Kanazawa, Microstructure and cavity swelling in reactor-irradiated dilute copper-boron alloy, J. Nucl. Mater. 179–181 (1991) 994–997, https://doi.org/10.1016/0022-3115(91)90258-9.

[57] S.J. Zinkle, G.L. Kulcinski, R.W. Knoll, Microstructure of copper following high dose 14-MeV Cu ion irradiation, J. Nucl. Mater. 138 (1986) 46–56, https://doi.org/10.1016/0022-3115(86)90254-0.

[58] S.J. Zinkle, In Effects of Radiation on Materials, 15th International Symposium, ASTM STF 1125; Stoller, R. E., et al., Eds.; ASTM: Philadelphia, PA, 1992; p 813., n.d.

[59] A.R. Raffray, J. Schlosser, M. Akiba, M. Araki, S. Chiocchio, D. Driemeyer, F. Escourbiac, S. Grigoriev, M. Merola, R. Tivey, G. Vieider, D. Youchison, Critical heat flux analysis and R&D for the design of the ITER divertor, Fusion Eng. Des. 45 (1999) 377–407, https://doi.org/10.1016/S0920-3796(99)00053-8.

[60] S.-E.-D. El-Morshedy, Thermal-hydraulic simulation of ITER tungsten divertor monoblock for loss of flow transient, Nucl. Mater. Energy 38 (2024) 101616, https://doi.org/10.1016/j.nme.2024.101616.

[61] M. Li, J.-H. You, Structural impact of creep in tungsten monoblock divertor target at 20 MW/m 2, Nucl. Mater. Energy 14 (2018) 1–7, https://doi.org/10.1016/j.nme.2017.12.001.

[62] J.W. Coenen, S. Antusch, M. Aumann, W. Biel, J. Du, J. Engels, S. Heuer, A. Houben, T. Hoeschen, B. Jasper, F. Koch, J. Linke, A. Litnovsky, Y. Mao, R. Neu, G. Pintsuk, J. Riesch, M. Rasinski, J. Reiser, M. Rieth, A. Terra, B. Unterberg, T. Weber, T. Wegener, J.-H. You, C. Linsmeier, Materials for DEMO and reactor applications—boundary conditions and new concepts, Phys. Scr. T167 (2016) 014002, https://doi.org/10.1088/0031-8949/2016/T167/014002.

[63] J. Habainy, Y. Dai, Y. Lee, S. Iyengar, Thermal diffusivity of tungsten irradiated with protons up to 5.8 dpa, J. Nucl. Mater. 509 (2018) 152–157, https://doi.org/10.1016/j.jnucmat.2018.06.041.

[64] J. Linke, P. Lorenzetto, P. Majerus, M. Merola, D. Pitzer, M. Rödig, EU Development of High Heat Flux Components, Fusion Sci. Technol. 47 (2005) 678–685. 10.13182/FST05-A764.

[65] M. Eldrup, B.N. Singh, Influence of composition, heat treatment and neutron irradiation on the electrical conductivity of copper alloys, J. Nucl. Mater. 258–263 (1998) 1022–1027, https://doi.org/10.1016/S0022-3115(98)00390-0.

[66] S. Wang, J. Li, Y. Wang, X. Zhang, R. Wang, Y. Wang, J. Cao, Thermal damage of tungsten-armored plasma-facing components under high heat flux loads, Sci. Rep. 10 (2020) 1359, https://doi.org/10.1038/s41598-020-57852-8.

[67] M. Fursdon, J.-H. You, Towards reliable design-by-analysis for divertor plasma facing components—Guidelines for inelastic assessment (part II: irradiated), Fusion Eng. Des. 160 (2020) 111831, https://doi.org/10.1016/j.fusengdes.2020.111831.

[68] A. Reza, H. Yu, K. Mizohata, F. Hofmann, Thermal diffusivity degradation and point defect density in self-ion implanted tungsten, Acta Mater. 193 (2020) 270–279, https://doi.org/10.1016/j.actamat.2020.03.034.

[69] D.R. Mason, A. Reza, F. Granberg, F. Hofmann, Estimate for thermal diffusivity in highly irradiated tungsten using molecular dynamics simulation, Phys. Rev. Mater. 5 (2021) 125407, https://doi.org/10.1103/PhysRevMaterials.5.125407.

[70] G. Sannazzaro, V. Barabash, S.C. Kang, E. Fernandez, G. Kalinin, A. Obushev, V. J. Martínez, I. Vázquez, F. Fernández, J. Guirao, Development of design Criteria for ITER In-vessel Components, Fusion Eng. Des. 88 (2013) 2138–2141, https://doi.org/10.1016/j.fusengdes.2013.01.019.

[71] M. Fursdon, J.-H. You, T. Barrett, M. Li, A hybrid analysis procedure enabling elastic design rule assessment of monoblock-type divertor components, Fusion Eng. Des. 135 (2018) 154–164, https://doi.org/10.1016/j.fusengdes.2018.07.014.
[72] H.L. Heinisch, The effects of low doses of 14 MeV neutrons on the tensile properties of three binary copper alloys, J. Nucl. Mater. 155–157 (1988) 1159–1163, https://doi.org/10.1016/0022-3115(88)90488-6.
[73] S.A. Fabritsiev, S.J. Zinkle, B.N. Singh, Evaluation of copper alloys for fusion reactor divertor and first wall components, J. Nucl. Mater. 233–237 (1996) 127–137, https://doi.org/10.1016/S0022-3115(96)00091-8.
[74] B.N. Singh, D.J. Edwards, A. Horsewell, P. Toft, Dose dependence of microstructural evolution and mechanical properties of neutron irradiated copper and copper alloys. (ITER R&D Task no. T13). Denmark. Forskningscenter Risoe. Risoe-R No. 839(EN), 1996, n.d.
[75] S.J. Zinkle, L.T. Gibson, Fusion Materials Semi-annual Progress; Report DOE/ER-0313/27; Oak Ridge National Laboratory, 1999; p 163., n.d.
[76] M. Richou, A. Durif, M. Lenci, M. Mondon, M. Minissale, L. Gallais, G. Kermouche, G. De Temmerman, Recrystallization at high temperature of two tungsten materials complying with the ITER specifications, J. Nucl. Mater. 542 (2020) 152418, https://doi.org/10.1016/j.jnucmat.2020.152418.
[77] L.M. Garrison, Y. Katoh, N.A.P.K. Kumar, Mechanical properties of single-crystal tungsten irradiated in a mixed spectrum fission reactor, J. Nucl. Mater. 518 (2019) 208–225, https://doi.org/10.1016/j.jnucmat.2019.02.050.